

2.4 Thermogravimetric Analysis

2.4.1 Thermogravimetric Analysis of Single Walled Carbon Nanotubes¹³

Thermogravimetric analysis (TGA) and the associated differential thermal analysis (DTA) are widely used for the characterization of both as-synthesized and side-wall functionalized single walled carbon nanotubes (SWNTs). Under oxygen, SWNTs will pyrolyze leaving any inorganic residue behind. In contrast in an inert atmosphere since most functional groups are labile or decompose upon heating and as SWNTs are stable up to 1200 °C, any weight loss before 800 °C is used to determine the functionalization ratio of side-wall functionalized SWNTs. The following properties of SWNTs can be determined using this TGA;

1. The mass of metal catalyst impurity in as synthesized SWNTs.
2. The number of functional groups per SWNT carbon (C_{SWNT}).
3. The mass of a reactive species absorbed by a functional group on a SWNT.

Quantitative determination of these properties are used to define the purity of SWNTs, and the extent of their functionalization.

2.4.1.1 An overview of thermogravimetric analysis

The main function of TGA is the monitoring of the thermal stability of a material by recording the change in mass of the sample with respect to temperature. Figure 2.47 shows a simple diagram of the inside of a typical TGA.

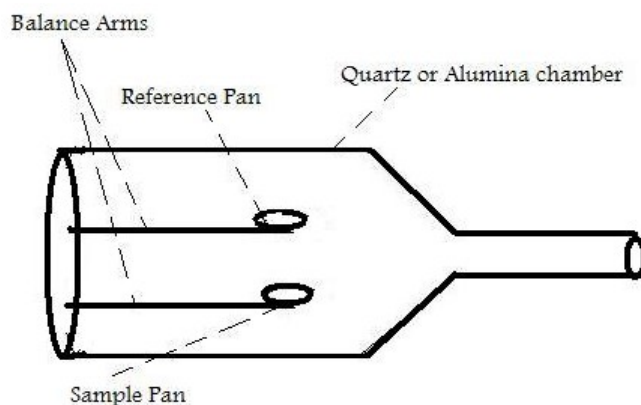


Figure 2.47: Schematic representation of a TGA apparatus.

Inside the TGA, there are two pans, a reference pan and a sample pan. The pan material can be either aluminium or platinum. The type of pan used depends on the maximum temperature of a given run. As platinum melts at 1760 °C and aluminium melts at 660 °C, platinum pans are chosen when the maximum temperature exceeds 660 °C. Under each pan there is a thermocouple which reads the temperature of the pan. Before the start of each run, each pan is balanced on a balance arm. The balance arms should be calibrated to compensate for the differential thermal expansion between the arms. If the arms are not calibrated, the instrument will only record the temperature at which an event occurred and not the change

¹³This content is available online at <<http://cnx.org/content/m22972/1.2/>>.

in mass at a certain time. To calibrate the system, the empty pans are placed on the balance arms and the pans are weighed and zeroed.

As well as recording the change in mass, the heat flow into the sample pan (differential scanning calorimetry, DSC) can also be measured and the difference in temperature between the sample and reference pan (differential thermal analysis, DTA). DSC is quantitative and is a measure of the total energy of the system. This is used to monitor the energy released and absorbed during a chemical reaction for a changing temperature. The DTA shows if and how the sample phase changed. If the DTA is constant, this means that there was no phase change. Figure 2.48 shows a DTA with typical examples of an exotherm and an endotherm.

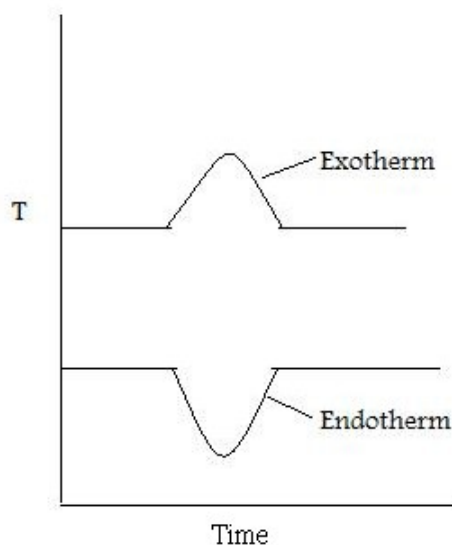


Figure 2.48: Simplified representation of the DTA for an exotherm and an endotherm.

When the sample melts, the DTA dips which signifies an endotherm. When the sample is melting it requires energy from the system. Therefore the temperature of the sample pan decreases compared with the temperature of the reference pan. When the sample has melted, the temperature of the sample pan increases as the sample is releasing energy. Finally the temperatures of the reference and sample pans equilibrate resulting in a constant DTA. When the sample evaporates, there is a peak in the DTA. This exotherm can be explained in the same way as the endotherm.

Typically the sample mass range should be between 0.1 to 10 mg and the heating rate should be 3 to 5 °C/min.

2.4.1.2 Determination of the mass of iron catalyst impurity in HiPco SWNTs.

SWNTs are typically synthesized using metal catalysts. Those prepared using the HiPco method, contain residual Fe catalyst. The metal (i.e., Fe) is usually oxidized upon exposure to air to the appropriate oxide (i.e., Fe_2O_3). While it is sometimes unimportant that traces of metal oxide are present during subsequent applications it is often necessary to quantify their presence. This is particularly true if the SWNTs are to be used for cell studies since it has been shown that the catalyst residue is often responsible for observed cellular toxicity.

In order to calculate the mass of catalyst residue the SWNTs are pyrolyzed under air or O₂, and the residue is assumed to be the oxide of the metal catalyst. Water can be added to the raw SWNTs, which enhances the low-temperature catalytic oxidation of carbon. A typical TGA plot of a sample of raw HiPco SWNTs is shown in Figure 2.49.

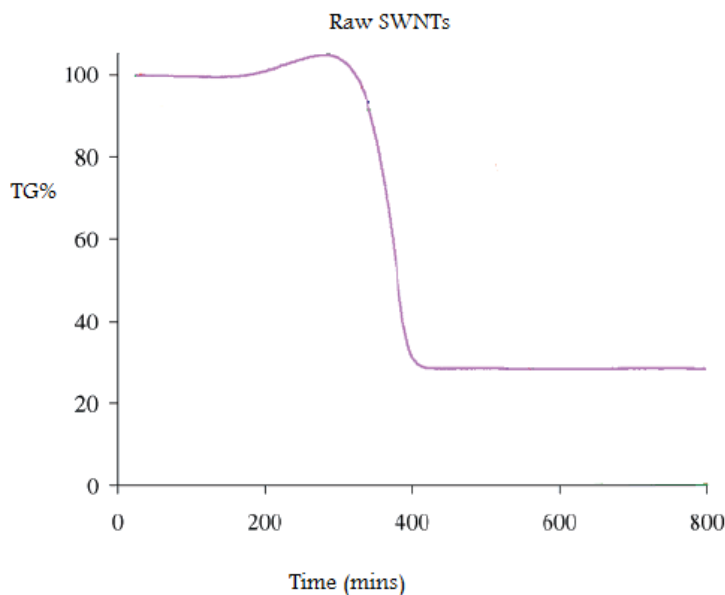


Figure 2.49: The TGA of unpurified HiPco SWNTs under air showing the residual mass associated with the iron catalyst. Adapted from I. W. Chiang, B. E. Brinson, A. Y. Huang, P. A. Willis, M. J. Bronikowski, J. L. Margrave, R. E. Smalley, and R. H. Hauge, *J. Phys. Chem. B*, 2001, **105**, 8297. Adapted from Chiang et al, 2001

The weight gain (of ca. 5%) at 300 °C is due to the formation of metal oxide from the incompletely oxidized catalyst. To determine the mass of iron catalyst impurity in the SWNT, the residual mass must be calculated. The residual mass is the mass that is left in the sample pan at the end of the experiment. From this TGA diagram, it is seen that 70% of the total mass is lost at 400 °C. This mass loss is attributed to the removal of carbon. The residual mass is 30%. Given that this is due to both oxide and oxidized metal, the original total mass of residual catalyst in raw HiPCO SWNTs is ca. 25%.

2.4.1.3 Determining the number of functional groups on SWNTs

The limitation of using SWNTs in any practical applications is their solubility; for example SWNTs have little to no solubility in most solvents due to aggregation of the tubes. Aggregation/roping of nanotubes occurs as a result of the high van der Waals binding energy of ca. 500 eV per μm of tube contact. The van der Waals force between the tubes is so great, that it takes tremendous energy to pry them apart, making it very difficult to make combination of nanotubes with other materials such as in composite applications. The functionalization of nanotubes, i.e., the attachment of “chemical functional groups”, provides the path to overcome these barriers. Functionalization can improve solubility as well as processability, and has been used to align the properties of nanotubes to those of other materials. In this regard, covalent functionalization

provides a higher degree of fine-tuning for the chemical and physical properties of SWNTs than non-covalent functionalization.

Functionalized nanotubes can be characterized by a variety of techniques, such as atomic force microscopy (AFM), transmission electron microscopy (TEM), UV-vis spectroscopy, and Raman spectroscopy, however, the quantification of the extent of functionalization is important and can be determined using TGA. Because any sample of functionalized-SWNTs will have individual tubes of different lengths (and diameters) it is impossible to determine the number of substituents per SWNT. Instead the extent of functionalization is expressed as number of substituents per SWNT carbon atom (C_{SWNT}), or more often as $C_{\text{SWNT}}/\text{substituent}$, since this is then represented as a number greater than 1.

Figure 2.50 shows a typical TGA for a functionalized SWNT. In this case it is polyethyleneimine (PEI) functionalized SWNTs prepared by the reaction of fluorinated SWNTs (F-SWNTs) with PEI in the presence of a base catalyst.

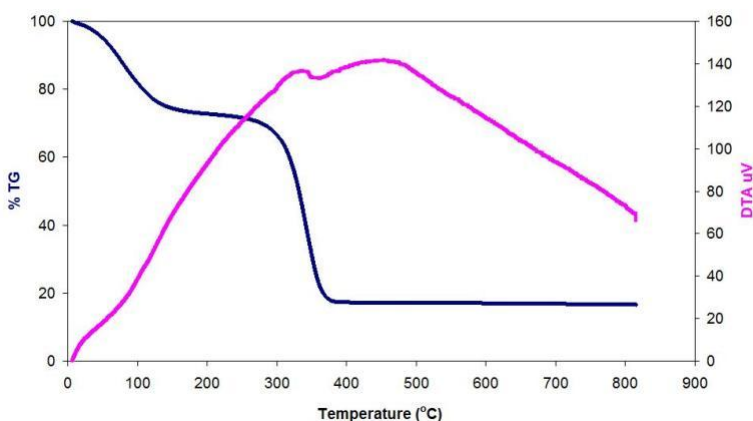


Figure 2.50: The TGA of SWNTs functionalized with polyethyleneimine (PEI) under air showing the sequential loss of complexed CO_2 and decomposition of PEI.

In the present case the molecular weight of the PEI is 600 g/mol. When the sample is heated, the PEI thermally decomposes leaving behind the unfunctionalized SWNTs. The initial mass loss below 100 °C is due to residual water and ethanol used to wash the sample.

In the following example the total mass of the sample is 25 mg.

- Step 1. The initial mass, $M_i = 25 \text{ mg} = \text{mass of the SWNTs, residues and the PEI}$.
- Step 2. After the initial moisture has evaporated there is 68% of the sample left. 68% of 25 mg is 17 mg. This is the mass of the PEI and the SWNTs.
- Step 3. At 300 °C the PEI starts to decompose and all of the PEI has been removed from the SWNTs at 370 °C. The mass loss during this time is 53% of the total mass of the sample. 53% of 25 mg is 13.25 mg.
- Step 4. The molecular weight of this PEI is 600 g/mol. Therefore there is $0.013 \text{ g} / 600 \text{ g/mol} = 0.022 \text{ mmole}$ of PEI in the sample.
- Step 5. 15% of the sample is the residual mass, this is the mass of the decomposed SWNTs. 15% of 25 mg is 3.75 mg. The molecular weight of carbon is 12 g/mol. So there is 0.3125 mmole of carbon in the sample.
- Step 6. There is 93.4 mol% of carbon and 6.5 mol% of PEI in the sample.

2.4.1.4 Determination of the mass of a chemical absorbed by functionalized SWNTs

Solid-state ^{13}C NMR of PEI-SWNTs shows the presence of carboxylate substituents that can be attributed to carbamate formation as a consequence of the reversible CO_2 absorption to the primary amine substituents of the PEI. Desorption of CO_2 is accomplished by heating under argon at 75°C .

The quantity of CO_2 absorbed per PEI-SWNT unit may be determined by initially exposing the PEI-SWNT to a CO_2 atmosphere to maximize absorption. The gas flow is switched to either Ar or N_2 and the sample heated to liberate the absorbed CO_2 without decomposing the PEI or the SWNTs. An example of the appropriate TGA plot is shown in Figure 2.51.

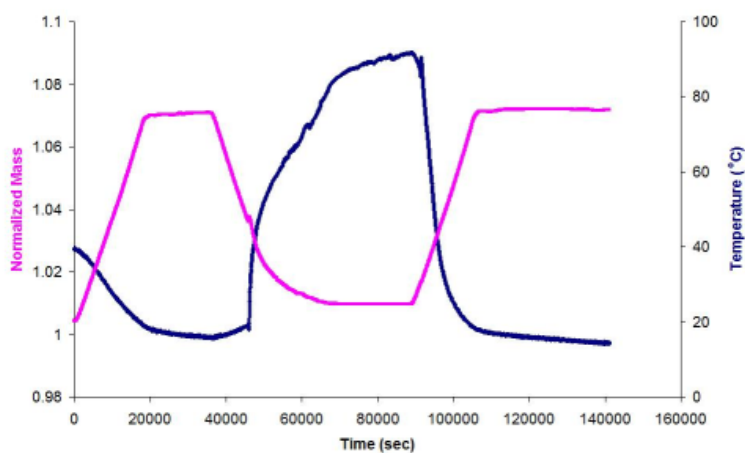


Figure 2.51: The TGA results of PEI(10000)-SWNT absorbing and desorbing CO_2 . The mass has been normalized to the lowest mass recorded, which is equivalent to PEI(10000)-SWNT.

The sample was heated to 75°C under Ar, and an initial mass loss due to moisture and/or atmospherically absorbed CO_2 is seen. In the temperature range of 25°C to 75°C the flow gas was switched from an inert gas to CO_2 . In this region an increase in mass is seen, the increase is due to CO_2 absorption by the PEI (10000Da)-SWNT. Switching the carrier gas back to Ar resulted in the desorption of the CO_2 .

The total normalized mass of CO_2 absorbed by the PEI(10000)-SWNT can be calculated as follows;

Solution Outline

- Step 1. Minimum mass = mass of absorbant = $M_{\text{absorbant}}$
- Step 2. Maximum mass = mass of absorbant and absorbed species = M_{total}
- Step 3. Absorbed mass = $M_{\text{absorbed}} = M_{\text{total}} - M_{\text{absorbant}}$
- Step 4. % of absorbed species = $(M_{\text{absorbed}}/M_{\text{absorbant}}) \times 100$
- Step 5. 1 mole of absorbed species = MW of absorbed species
- Step 6. Number of moles of absorbed species = $(M_{\text{absorbed}}/\text{MW of absorbed species})$
- Step 7. The number of moles of absorbed species absorbed per gram of absorbant = $(1\text{g}/M_{\text{total}}) \times (\text{Number of moles of absorbed species})$

Solution

- Step 1. $M_{\text{absorbant}} = \text{Mass of PEI-SWNT} = 4.829 \text{ mg}$
- Step 2. $M_{\text{total}} = \text{Mass of PEI-SWNT and } \text{CO}_2 = 5.258 \text{ mg}$

- Step 3. $M_{\text{absorbed}} = M_{\text{total}} - M_{\text{absorbant}} = 5.258 \text{ mg} - 4.829 \text{ mg} = 0.429 \text{ mg}$
 Step 4. % of absorbed species = % of CO_2 absorbed = $(M_{\text{absorbed}}/M_{\text{absorbant}})*100 = (0.429/4.829)*100 = 8.8\%$
 Step 5. 1 mole of absorbed species = MW of absorbed species = MW of $\text{CO}_2 = 44$ therefore 1 mole = 44g
 Step 6. Number of moles of absorbed species = $(M_{\text{absorbed}}/\text{MW of absorbed species}) = (0.429 \text{ mg} / 44 \text{ g}) = 9.75 \mu\text{M}$
 Step 7. The number of moles of absorbed species absorbed per gram of absorbant = $(1 \text{ g}/M_{\text{total}})*(\text{Number of moles of absorbed species}) = (1 \text{ g}/5.258 \text{ mg})*(9.75) = 1.85 \text{ mmol of CO}_2 \text{ absorbed per gram of absorbant}$

2.4.1.5 Bibliography

- I. W. Chiang, B. E. Brinson, A. Y. Huang, P. A. Willis, M. J. Bronikowski, J. L. Margrave, R. E. Smalley, and R. H. Hauge, *J. Phys. Chem. B*, 2001, **105**, 8297.
- E. P. Dillon, C. A. Crouse and A. R. Barron, *ACS Nano*, 2008, **2**, 156.

2.4.2 TGA/DSC-FTIR Characterization of Oxide Nanoparticles¹⁴

2.4.2.1 Metal oxide nanoparticles

The binary compound of one or more oxygen atoms with at least one metal atom that forms a structure $\leq 100 \text{ nm}$ is classified as metal oxide (MO_x) nanoparticle. MO_x nanoparticles have exceptional physical and chemical properties (especially if they are smaller than 10 nm) that are strongly related to their dimensions and to their morphology. These enhanced features are due to the increased surface to volume ratio which has a strong impact on the measured binding energies. Based on theoretical models, binding or cohesive energy is inversely related to particle size with a linear relationship (2.45).

$$E_{\text{NP}} = E_{\text{bulk}} \cdot [1 - c \cdot r^{-1}] \quad (2.45)$$

where E_{NP} and E_{bulk} is the binding energy of the nanoparticle and the bulk binding energy respectively, c is a material constant and r is the radius of the cluster. As seen from (2.45), nanoparticles have lower binding energies than bulk material, which means lower electron cloud density and therefore more mobile electrons. This is one of the features that have been identified to contribute to a series of physical and chemical properties.

2.4.2.1.1 Synthesis of metal oxide nanoparticles

Since today, numerous synthetic methods have been developed with the most common ones presented in Table 2.5. These methods have been successfully applied for the synthesis of a variety of materials with 0-D to 3-D complex structures. Among them, the solvothermal methods are by far the most popular ones due to their simplicity. Between the two classes of solvothermal methods, slow decomposition methods, usually called thermal decomposition methods, are preferred over the hot injection methods since they are less complicated, less dangerous and avoid the use of additional solvents.

Method	Characteristics	Advantages	Disadvantages
<i>continued on next page</i>			

¹⁴This content is available online at <<http://cnx.org/content/m23038/1.2/>>.

Solvothermal a) Slow decomposition b) Hot injection	a) Slow heating of M-precursor in the presence of ligand/surfactant precursor b) Injection of M-precursor into solution at high Temp.	a) Safe, easily carried out, variety of M-precursors to use b) Excellent control of particle distribution	a) Poor control of nucleation/growth stages – Particle size b) Hazardous, Reproducibility depends on individual
Template directed	Use of organic molecules or preexistent nanoparticles as templates for directing nanoparticle formation	High yield and high purity of nanoparticles	Template removal in some cases causes particle deformation or loss
Sonochemical	Ultrasound influence particle nucleation	Mild synthesis conditions	Limited applicability
Thermal evaporation	Thermal evaporation of Metal oxides	Monodisperse particle formation, excellent control in shape and structure	Extremely high temperatures, and vacuum system is required
Gas phase catalytic growth	Use of catalyst that serves as a preferential site for absorbing Metal reactants	Excellent control in shape and structure	Limited applicability

Table 2.5: Methods for synthesizing MO_x nanoparticles

A general schematic diagram of the stages involving the nanoparticles formation is shown in Figure 2.52. As seen, first step is the M-atom generation by dissociation of the metal-precursor. Next step is the M-complex formulation, which is carried out before the actual particle assembly stage. Between this step and the final particle formulation, oxidation of the activated complex occurs upon interaction with an oxidant substance. The x-axis is a function of temperature or time or both depending on the synthesis procedure.

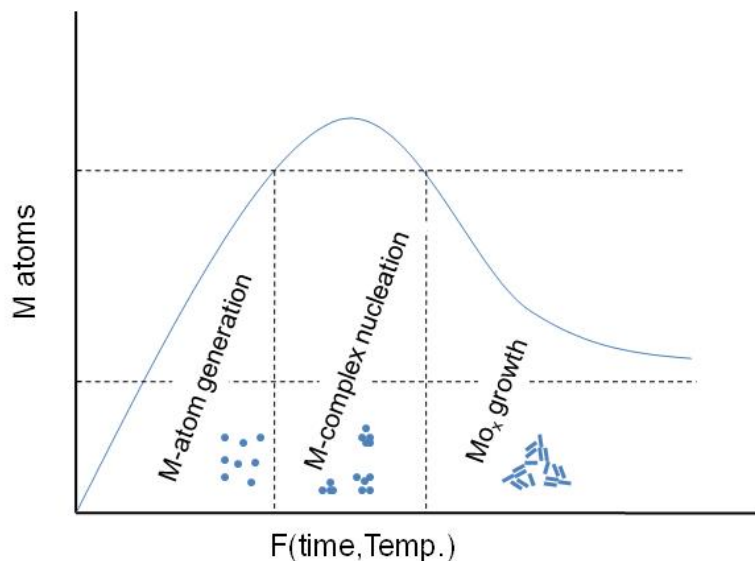


Figure 2.52: Stages of nanoparticle synthesis.

In all cases, the particles synthesized consist of MO_x nanoparticle structures stabilized by one or more types of ligand(s) as seen in Figure 2.53. The ligands are usually long-chained organic molecules that have one or more functional groups. These molecules protect the nanoparticles from attracting each other under van der Waals forces and therefore prevent them from aggregating.

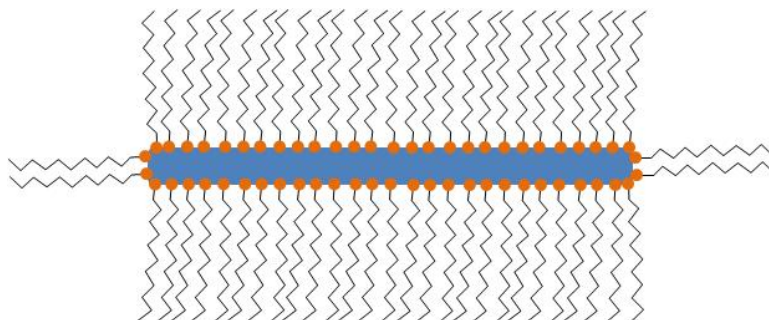


Figure 2.53: Schematic representation of a surfactant/ligand stabilized nanoparticle.

Even though often not referred to specifically, all particles synthesized are stabilized by organic (hydrophilic, hydrophobic or amphoteric) ligands. The detection and the understanding of the structure of these ligands can be of critical importance for understanding the controlling the properties of the synthesized nanoparticles.

2.4.2.1.1.1 Metal oxide nanoparticles synthesized via slow decomposition

In this work, we refer to MO_x nanoparticles synthesized via slow decomposition of a metal complex. In Table 2.6, a number of different MO_x nanoparticles are presented, synthesized via metal complex dissociation. Metal- MO_x and mixed MO_x nanoparticles are not discussed here.

Metal oxide	Shape	Size (approx.)
Cerium oxide	dots	5-20 nm
Iron oxide	dots, cubes	8.5-23.4 nm
Manganese oxide	Multipods	>50 nm
Zinc oxide	Hexagonal pyramid	15-25 nm
Cobalt oxide	dots	~ 10 nm
Chromium oxide	dots	12 nm
Vanadium oxide	dots	9-15 nm
Molybdenum oxide	dots	5 nm
Rhodium oxide	dots, rods	16 nm
Palladium oxide	dots	18 nm
Ruthenium oxide	dots	9-14 nm
Zirconium oxide	rods	7x30 nm
Barium oxide	dots	20 nm
Magnesium oxide	dots	4-8 nm
Calcium oxide	dots, rods	7-12 nm
Nickel oxide	dots	8-15 nm
Titanium oxide	dots and rods	2.3-30 nm
Tin oxide	dots	2.0-5.0 nm
Indium oxide	dots	~ 5 nm
Samaria	Square	~ 10 nm

Table 2.6: Examples of MO_x nanoparticles synthesized via decomposition of metal complexes.

A significant number of metal oxides synthesized using slow decomposition is reported in literature. If we use the periodic table to map the different MO_x nanoparticles (Figure 2.54), we notice that most of the alkali and transition metals generate MO_x nanoparticles, while only a few of the poor metals seem to do so, using this synthetic route. Moreover, two of the rare earth metals (Ce and Sm) have been reported to successfully give metal oxide nanoparticles via slow decomposition.

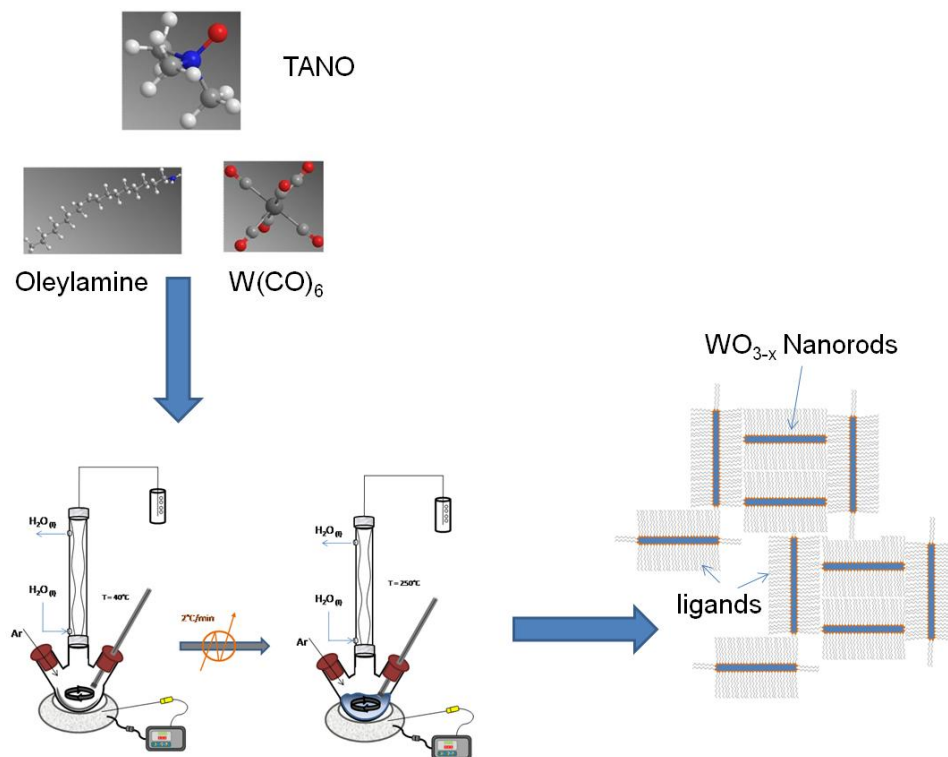


Figure 2.55: Experimental setup for synthesis of WO_{3-x} nanorods.

Multiple color variations were observed between 100 - 250 °C with the final product having a dark blue color. Tungsten oxide nanorods ($\text{W}_{18}\text{O}_{49}$ identified by XRD) with a diameter of 7 ± 2 nm and 50 ± 2 nm long were acquired after centrifugation of the product solution. A TEM image of the $\text{W}_{18}\text{O}_{49}$ nanorods is shown in Figure 2.56.

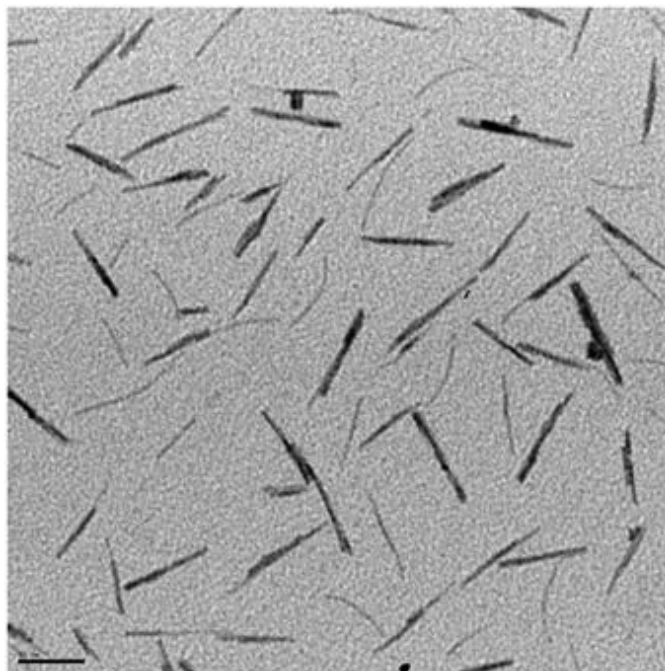


Figure 2.56: TEM image of WO_{3-x} nanorods.

2.4.2.2 Thermogravimetric analysis (TGA)/differential scanning calorimetry (DSC)

Thermogravimetric analysis (TGA) is a technique widely used for determining the organic and inorganic content of various materials. Its basic rule of function is the high precision measurement of weight gain/loss with increasing temperature under inert or reactive atmospheres. Each weight change corresponds to physical (crystallization, phase transformation) or chemical (oxidation, reduction, reaction) processes that take place by increasing the temperature. The sample is placed into platinum or alumina pan and along with an empty or standard pan are placed onto two high precision balances inside a high temperature oven. A method for pretreating the samples is selected and the procedure is initiated. Differential scanning calorimetry (DSC) is a technique usually accompanying TGA and is used for calculating enthalpy energy changes or heat capacity changes associated with phase transitions and/or ligand-binding energy cleavage.

In Figure 2.57 the TGA/DSC plot acquired for the ligand decomposition of WO_{3-x} nanorods is presented. The sample was heated at constant rate under N_2 atmosphere up to 195 °C for removing moisture and then up to 700 °C for removing the oleylamine ligands. It is important to use an inert gas for performing such a study to avoid any premature oxidation and/or capping agent combustion. 26.5% of the weight loss is due to oleylamine evaporations which means about 0.004 moles per gram of sample. After isothermal heating at 700 °C for 25 min the flow was switched to air for oxidizing the ligand-free WO_{3-x} to WO_3 . From the DSC curve we noticed the following changes of the weight corrected heat flow:

1. From 0 – 10 min assigned to water evaporation.
2. From 65 – 75 min assigned to OA evaporation.
3. From 155 – 164 min assigned to WO_{3-x} oxidation.
4. From 168 – 175 min is also due to further oxidation of W^{5+} atoms.

The heat flow increase during the WO_{3-x} to WO_3 oxidation is proportional to the crystal phase defects (or W atoms of oxidation state +5) and can be used for performing qualitative studies between different WO_x nanoparticles.

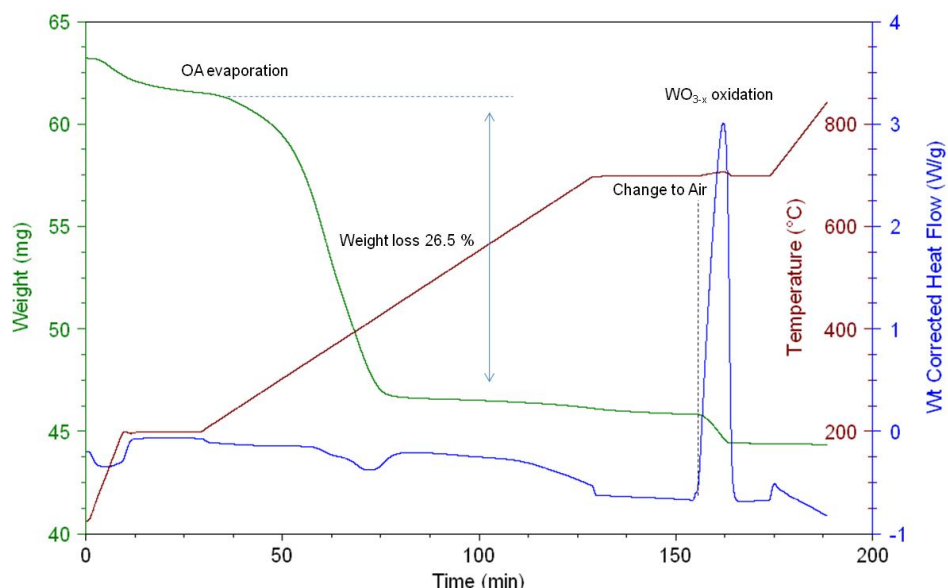


Figure 2.57: TGA/DSC plot for WO_{3-x} nanorods.

The detailed information about the procedure used to acquire the TGA/DSC plot shown in Figure 2.57 is as follows.

- Step 1. Select gas (N_2 with flow rate 50 mL/min.)
- Step 2. Ramp 20 °C/min to 200 °C.
- Step 3. Isothermal for 20 min.
- Step 4. Ramp 5 °C/min to 700 °C.
- Step 5. Isothermal for 25 min.
- Step 6. Select gas (air).
- Step 7. Isothermal for 20 min.
- Step 8. Ramp 10 °C/min to 850 °C.
- Step 9. Cool down

2.4.2.3 Fourier transform infrared spectroscopy

Fourier transform infrared spectroscopy (FTIR) is the most popular spectroscopic method used for characterizing organic and inorganic compounds. The basic modification of an FTIR from a regular IR instrument is a device called interferometer, which generates a signal that allows very fast IR spectrum acquisition. For doing so, the generated interferogram has to be “expanded” using a Fourier transformation to generate a

complete IR frequency spectrum. In the case of performing FTIR transmission studies the intensity of the transmitted signal is measured and the IR fingerprint is generated (2.46).

$$T = \frac{I}{I_b} = e^{c\epsilon l} \quad (2.46)$$

Where I is the intensity of the samples, I_b is the intensity of the background, c is the concentration of the compound, ϵ is the molar extinction coefficient and l is the distance that light travels through the material. A transformation of transmission to absorption spectra is usually performed and the actual concentration of the component can be calculated by applying the Beer-Lambert law (2.47).

$$A = -\ln(T) = c\epsilon l \quad (2.47)$$

A qualitative IR-band map is presented in Figure 2.58. The absorption bands between 4000 to 1600 cm^{-1} represent the group frequency region and are used to identify the stretching vibrations of different bonds. At lower frequencies (from 1600 to 400 cm^{-1}) vibrations due to intermolecular bond bending occurs upon IR excitation and therefore are usually not taken into account.

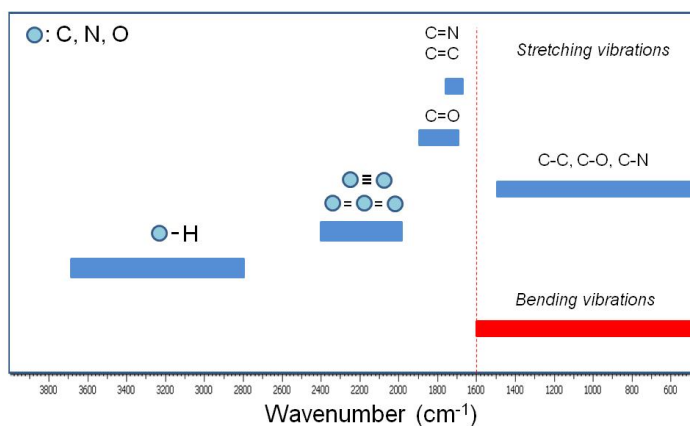


Figure 2.58: Selected FTIR stretching and bending modes associated with the typical ligands used for nanoparticle stabilization.

2.4.2.4 TGA/DSC–FTIR characterization

TGA/DSC is a powerful tool for identifying the different compounds evolved during the controlled pyrolysis and therefore provide qualitative and quantitative information about the volatile components of the sample. In metal oxide nanoparticle synthesis TGA/DSC-FTIR studies can provide qualitative and quantitative information about the volatile compounds of the nanoparticles.

TGA–FTIR results presented below were acquired using a Q600 Simultaneous TGA/DSC (SDT) instrument online with a Nicolet 5700 FTIR spectrometer. This system has a digital mass flow control and two gas inlets giving the capability to switch reacting gas during each run. It allows simultaneous weight change and differential heat flow measurements up to 1500 °C, while at the same time the outflow line is connected to the FTIR for performing gas phase compound identification. Grand-Schmidt thermographs were usually constructed to present the species evolution with time in 3 dimensions.

Selected IR spectra are presented in Figure 2.59. Four regions with intense peaks are observed. Between $4000 - 3550 \text{ cm}^{-1}$ due to O-H bond stretching assigned to H_2O that is always present and due to due to N-H group stretching that is assigned to the amine group of oleylamine. Between $2400 - 2250 \text{ cm}^{-1}$ due to $\text{O}=\text{C}=\text{O}$ stretching, between $1900 - 1400 \text{ cm}^{-1}$ which is mainly to C=O stretching and between $800 - 400 \text{ cm}^{-1}$ cannot be resolved as explained previously.

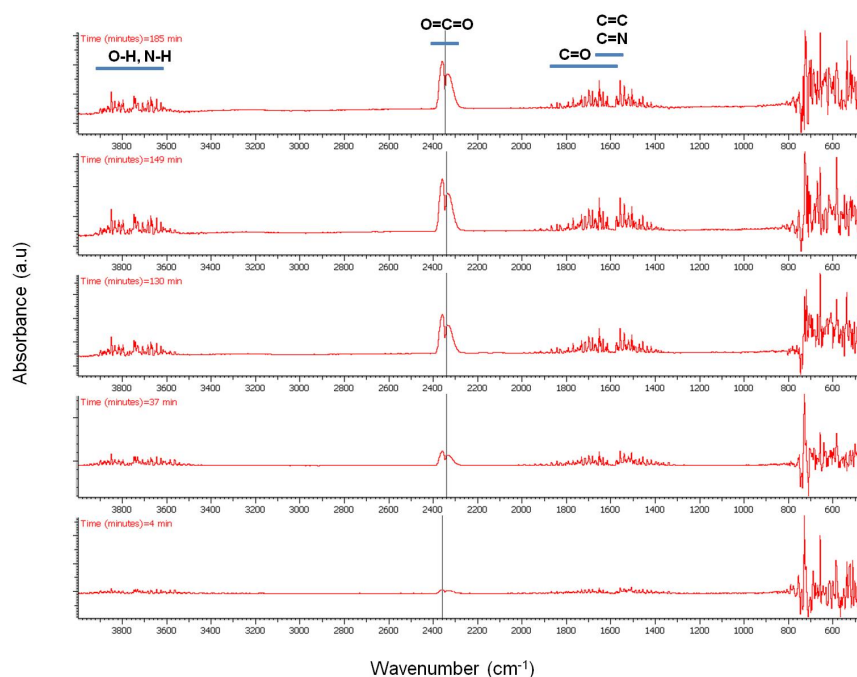


Figure 2.59: FTIR spectra of products from WO_{3-x} pyrolysis.

The peak intensity evolution with time can be more easily observed in Figure 2.60 and Figure 2.61. As seen, CO_2 evolution increases significantly with time especially after switching our flow from N_2 to air. H_2O seems to be present in the outflow stream up to $700 \text{ }^\circ\text{C}$ while the majority of the N-H amine peaks seem to disappear at about 75 min. C=N compounds are not expected to be present in the stream which leaves bands between $1900 - 1400 \text{ cm}^{-1}$ assigned to C=C and C=O stretching vibrations. Unsaturated olefins resulting from the cracking of the oleylamine molecule are possible at elevated temperatures as well as the presence of CO especially under N_2 atmosphere.

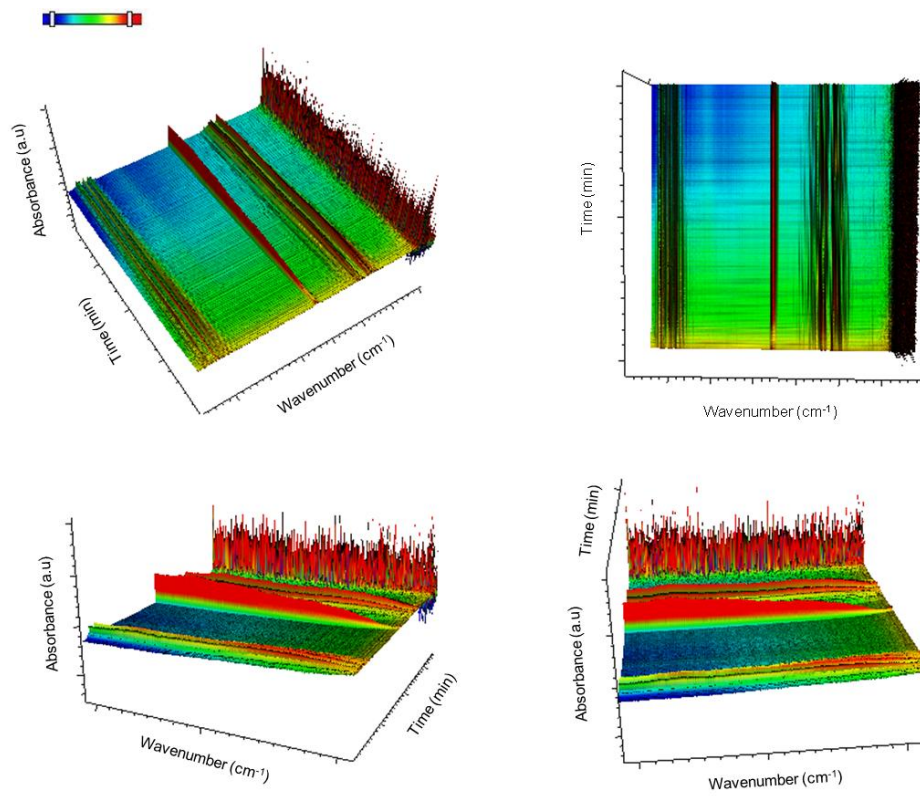


Figure 2.60: 3D representation of FTIR Spectra of the volatile compounds of WO_{3-x} .

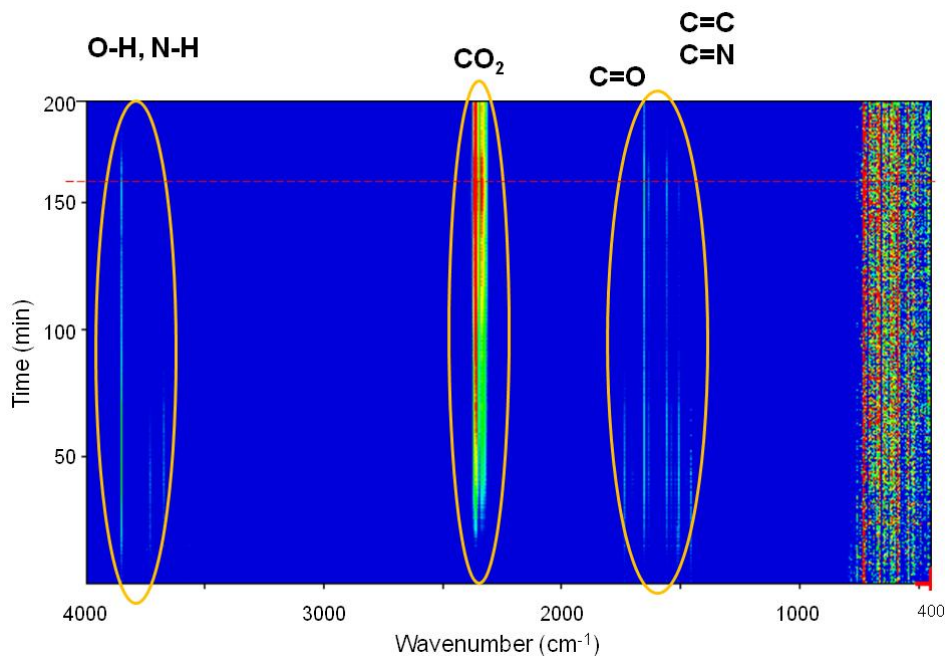


Figure 2.61: Intensity profile of FTIR spectra of the volatile compounds formed from the pyrolysis of WO_{3-x} .

From the above compound identification we can summarize and propose the following applications for TGA-FTIR. First, more complex ligands, containing aromatic rings and maybe other functional groups may provide more insight in the ligand to MO_x interaction. Second, the presence of CO and CO_2 even under N_2 flow means that complete O_2 removal from the TGA and the FTIR cannot be achieved under these conditions. Even though the system was equilibrated for more than an hour, traces of O_2 are existent which create errors in our calculations.

2.4.2.5 Bibliography

- R. D. Parra and H. H. Farrell, *J. Phys. Chem. C*, 2009, **113**, 4786.
- S. C. Vanithakumari and K. K. Nanda, *J. Phys. Chem. B*, 2006, **110**, 6985.
- M. Wautelet and D. Duvivier, *Eur. J. Phys.*, 2007, **28**, 953.
- X. Wang and Y. Li, *J. Am. Chem. Soc.*, 2002, **124**, 2880.
- F. K. R. N. Greta and R. Patzke, *Angew. Chem., Int. Ed.*, 2002, **41**, 2446.
- Z. W. Pan, Z. R. Dai, and Z. L. Wang, *Science*, 2001, **291**, 1947.
- H. Gu and M. D. Soucek, *Chem. Mater.*, 2007, **19**, 1103.
- L. M. Bronstein, X. Huang, J. Retrum, A. Schmucker, M. Pink, B. D. Stein, and B. Dragnea, *Chem. Mater.*, 2007, **19**, 3624.
- D. Zitoun, N. Pinna, N. Frolet, and C. Belin, *J. Am. Chem. Soc.*, 2005, **127**, 15034.
- S. -H. Choi, E. -G. Kim, J. Park, K. An, N. Lee, S. C. Kim, and T. Hyeon, *J. Phys. Chem., B*, 2005, **109**, 14792.
- M. Epifani, J. Arbiol, R. Diaz, M. J. Peralvarez, P. Siciliano, and J. R. Morante, *Chem. Mater.*, 2005, **17**, 6468.

- T. Yu, J. Joo, Y. I. Park, and T. Hyeon, *J. Am. Chem. Soc.*, 2006, **128**, 1786.
- K. Lee, W. S. Seo, and J. T. Park, *J. Am. Chem. Soc.*, 2003, **125**, 3408.
- C. A. Emeis, *J. Catalysis*, 1993, **141**, 347.
- P. R. Griffiths, J. A. De Haseth, *Fourier Transform Infrared Spectrometry*. Wiley-Interscience, New York (2007)

2.4.3 Determination of Sublimation Enthalpy and Vapor Pressure for Inorganic and Metal-Organic Compounds by Thermogravimetric Analysis¹⁵

2.4.3.1 Introduction

Metal compounds and complexes are invaluable precursors for the chemical vapor deposition (CVD) of metal and non-metal thin films. In general, the precursor compounds are chosen on the basis of their relative volatility and their ability to decompose to the desired material under a suitable temperature regime. Unfortunately, many readily obtainable (commercially available) compounds are not of sufficient volatility to make them suitable for CVD applications. Thus, a *prediction* of the volatility of a metal-organic compounds as a function of its ligand identity and molecular structure would be desirable in order to determine the suitability of such compounds as CVD precursors. Equally important would be a method to determine the vapor pressure of a potential CVD precursor as well as its optimum temperature of sublimation.

It has been observed that for organic compounds it was determined that a rough proportionality exists between a compound's melting point and sublimation enthalpy; however, significant deviation is observed for inorganic compounds.

Enthalpies of sublimation for metal-organic compounds have been previously determined through a variety of methods, most commonly from vapor pressure measurements using complex experimental systems such as Knudsen effusion, temperature drop microcalorimetry and, more recently, differential scanning calorimetry (DSC). However, the measured values are highly dependent on the experimental procedure utilized. For example, the reported sublimation enthalpy of $\text{Al}(\text{acac})_3$ (Figure 2.62a, where $M = \text{Al}$, $n = 3$) varies from 47.3 to 126 kJ/mol.

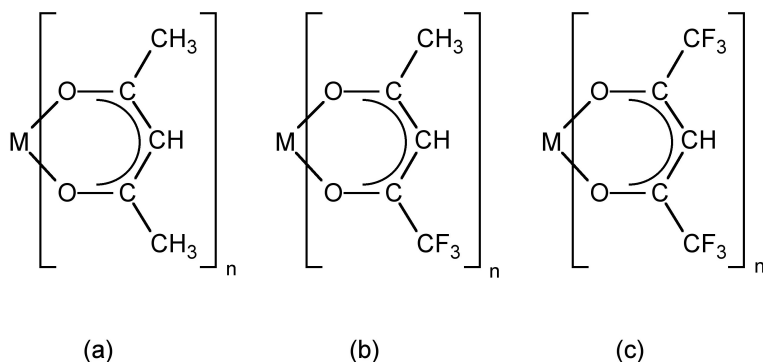


Figure 2.62: Structure of a typical metal β -diketonate complex. (a) acetylacetonate (acac); (b) trifluoroacetylacetonate (tfac), and (c) hexafluoroacetylacetonate (hfac).

Thermogravimetric analysis offers a simple and reproducible method for the determination of the vapor pressure of a potential CVD precursor as well as its enthalpy of sublimation.

¹⁵This content is available online at <<http://cnx.org/content/m33649/1.2/>>.

2.4.3.2 Determination of sublimation enthalpy

The enthalpy of sublimation is a quantitative measure of the volatility of a particular solid. This information is useful when considering the feasibility of a particular precursor for CVD applications. An ideal sublimation process involves no compound decomposition and only results in a solid-gas phase change, i.e., (2.48).



Since phase changes are thermodynamic processes following zero-order kinetics, the evaporation rate or rate of mass loss by sublimation (m_{sub}), at a constant temperature (T), is constant at a given temperature, (2.49). Therefore, the m_{sub} values may be directly determined from the linear mass loss of the TGA data in isothermal regions.

$$m_{\text{sub}} = \frac{\Delta[\text{mass}]}{\Delta t} \quad (2.49)$$

The thermogravimetric and differential thermal analysis of the compound under study is performed to determine the temperature of sublimation and thermal events such as melting. Figure 2.63 shows a typical TG/DTA plot for a gallium chalcogenide cubane compound (Figure 2.64).

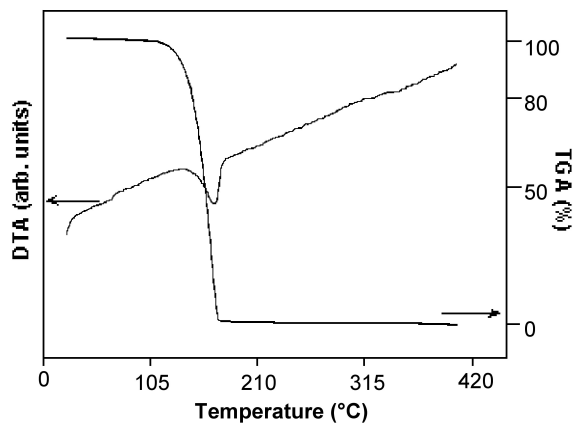


Figure 2.63: A typical thermogravimetric/differential thermal analysis (TG/DTA) analysis of $[(\text{EtMe}_2\text{C})\text{GaSe}]_4$, whose structure is shown in Figure 2.64. Adapted from E. G. Gillan, S. G. Bott, and A. R. Barron, *Chem. Mater.*, 1997, **9**, 3, 796.

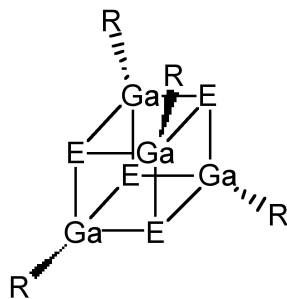


Figure 2.64: Structure of gallium chalcogenide cubane compound, where E = S, Se, and R = CMe₃, CMe₂Et, CEt₂Me, CEt₃.

2.4.3.2.1 Data collection

In a typical experiment 5 - 10 mg of sample is used with a heating rate of ca. 5 °C/min up to under either a 200-300 mL/min inert (N₂ or Ar) gas flow or a dynamic vacuum (ca. 0.2 Torr if using a typical vacuum pump). The argon flow rate was set to 90.0 mL/min and was carefully monitored to ensure a steady flow rate during runs and an identical flow rate from one set of data to the next.

Once the temperature range is defined, the TGA is run with a preprogrammed temperature profile (Figure 2.65). It has been found that sufficient data can be obtained if each isothermal mass loss is monitored over a period (between 7 and 10 minutes is found to be sufficient) before moving to the next temperature plateau. In all cases it is important to confirm that the mass loss at a given temperature is linear. If it is not, this can be due to either (a) temperature stabilization had not occurred and so longer times should be spent at each isotherm, or (b) decomposition is occurring along with sublimation, and lower temperature ranges must be used. The slope of each mass drop is measured and used to calculate sublimation enthalpies as discussed below.

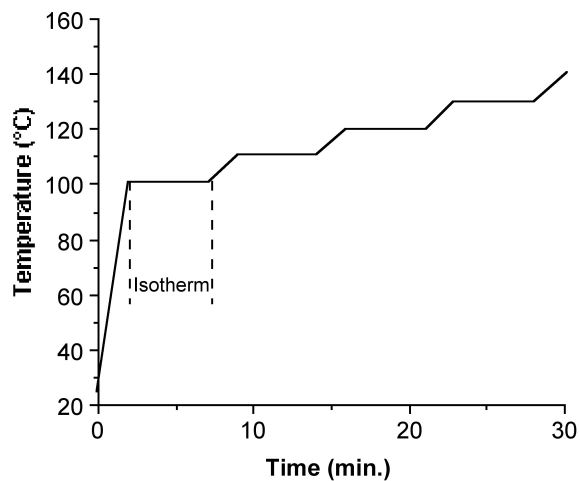


Figure 2.65: A typical temperature profile for determination of isothermal mass loss rate.

As an illustrative example, Figure 2.66 displays the data for the mass loss of $\text{Cr}(\text{acac})_3$ (Figure 2.62a, where $M = \text{Cr}$, $n = 3$) at three isothermal regions under a constant argon flow. Each isothermal data set should exhibit a linear relation. As expected for an endothermal phase change, the linear slope, equal to m_{sub} , increases with increasing temperature.

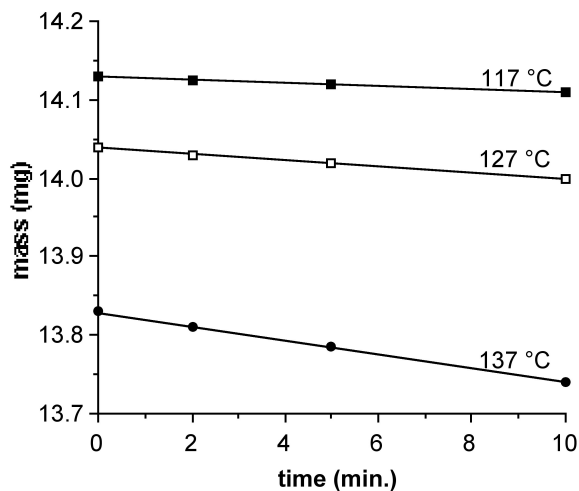


Figure 2.66: Plot of TGA results for $\text{Cr}(\text{acac})_3$ performed at different isothermal regions. Adapted from B. D. Fahlman and A. R. Barron, *Adv. Mater. Optics Electron.*, 2000, **10**, 223.

NOTE: Samples of iron acetylacetonate (Figure 2.62a, where $M = \text{Fe}$, $n = 3$) may be used as a calibration standard through ΔH_{sub} determinations before each day of use. If the measured value of the sublimation enthalpy for $\text{Fe}(\text{acac})_3$ is found to differ from the literature value by more than 5%, the sample is re-analyzed and the flow rates are optimized until an appropriate value is obtained. Only after such a calibration is optimized should other complexes be analyzed. It is important to note that while small amounts ($< 10\%$) of involatile impurities will not interfere with the ΔH_{sub} analysis, competitively volatile impurities will produce higher apparent sublimation rates.

It is important to discuss at this point the various factors that must be controlled in order to obtain meaningful (useful) m_{sub} data from TGA data.

1. The sublimation rate is independent of the amount of material used but may exhibit some dependence on the flow rate of an inert carrier gas, since this will affect the equilibrium concentration of the cubane in the vapor phase. While little variation was observed we decided that for consistency m_{sub} values should be derived from vacuum experiments only.
2. The surface area of the solid in a given experiment should remain approximately constant; otherwise the sublimation rate (i.e., mass/time) at different temperatures cannot be compared, since as the relative surface area of a given crystallite decreases during the experiment the apparent sublimation rate will also decrease. To minimize this problem, data was taken over a small temperature ranges (ca. 30 °C), and overall sublimation was kept low (ca. 25% mass loss representing a surface area change of less than 15%). In experiments where significant surface area changes occurred the values of m_{sub} deviated significantly from linearity on a $\log(m_{\text{sub}})$ versus $1/T$ plot.
3. The compound being analyzed must not decompose to any significant degree, because the mass changes due to decomposition will cause a reduction in the apparent m_{sub} value, producing erroneous results. With a simultaneous TG/DTA system it is possible to observe exothermic events if decomposition occurs, however the clearest indication is shown by the mass loss versus time curves which are no longer linear but exhibit exponential decays characteristic of first or second order decomposition processes.

2.4.3.2.2 Data analysis

The basis of analyzing isothermal TGA data involves using the Clausius-Clapeyron relation between vapor pressure (p) and temperature (T), (2.50), where ΔH_{sub} is the enthalpy of sublimation and R is the gas constant (8.314 J/K.mol).

$$\frac{d \ln(p)}{dT} = \frac{\Delta H_{\text{sub}}}{RT^2} \quad (2.50)$$

Since m_{sub} data are obtained from TGA data, it is necessary to utilize the Langmuir equation, (2.51), that relates the vapor pressure of a solid with its sublimation rate.

$$p = \left[\frac{2\pi RT}{M_w} \right]^{0.5} m_{\text{sub}} \quad (2.51)$$

After integrating (2.50) in log form, substituting in (2.51), and consolidating the constants, one obtains the useful equality, (2.52).

$$\log(m_{\text{sub}}\sqrt{T}) = \frac{-0.0522(\Delta H_{\text{sub}})}{T} + \left[\frac{0.0522(\Delta H_{\text{sub}})}{T_{\text{sub}}} - \frac{1}{2} \log\left(\frac{1306}{M_w}\right) \right] \quad (2.52)$$

Hence, the linear slope of a $\log(m_{\text{sub}}T^{1/2})$ versus $1/T$ plot yields ΔH_{sub} . An example of a typical plot and the corresponding ΔH_{sub} value is shown in Figure 2.67. In addition, the y intercept of such a plot provides a value for T_{sub} , the calculated sublimation temperature at atmospheric pressure.

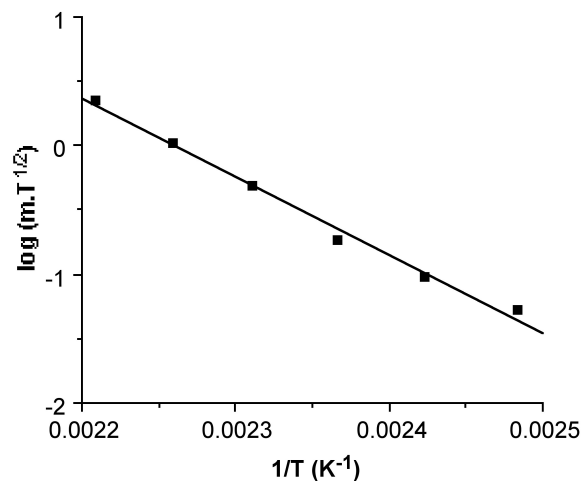


Figure 2.67: Plot of $\log(m_{\text{sub}}T^{1/2})$ versus $1/T$ and the determination of the ΔH_{sub} (112.6 kJ/mol) for $\text{Fe}(\text{acac})_3$ ($R^2 = 0.9989$). Adapted from B. D. Fahlman and A. R. Barron, *Adv. Mater. Optics Electron.*, 2000, **10**, 223.

Table 2.7 lists the typical results using the TGA method for a variety of metal β -diketonates, while Table 2.8 lists similar values obtained for gallium chalcogenide cubane compounds.

Compound	ΔH_{sub} (kJ/mol)	ΔS_{sub} (J/K.mol)	T_{sub} calc. ($^{\circ}\text{C}$)	Calculated vapor pressure @ 150 $^{\circ}\text{C}$ (Torr)
$\text{Al}(\text{acac})_3$	93	220	150	3.261
$\text{Al}(\text{tfac})_3$	74	192	111	9.715
$\text{Al}(\text{hfac})_3$	52	152	70	29.120
$\text{Cr}(\text{acac})_3$	91	216	148	3.328
$\text{Cr}(\text{tfac})_3$	71	186	109	9.910
$\text{Cr}(\text{hfac})_3$	46	134	69	29.511
$\text{Fe}(\text{acac})_3$	112	259	161	2.781
$\text{Fe}(\text{tfac})_3$	96	243	121	8.340

continued on next page

Fe(hfac) ₃	60	169	81	25.021
Co(acac) ₃	138	311	170	1.059
Co(tfac) ₃	119	295	131	3.319
Co(hfac) ₃	73	200	90	9.132

Table 2.7: Selected thermodynamic data for metal β -diketonate compounds determined from thermogravimetric analysis. Data from B. D. Fahlman and A. R. Barron, *Adv. Mater. Optics Electron.*, 2000, **10**, 223.

Compound	ΔH_{sub} (kJ/mol)	ΔS_{sub} (J/K.mol)	T_{sub} calc. ($^{\circ}\text{C}$)	Calculated vapor pressure @ 150 $^{\circ}\text{C}$ (Torr)
[(Me ₃ C)GaS] ₄	110	300	94	22.75
[(EtMe ₂ C)GaS] ₄	124	330	102	18.89
[(Et ₂ MeC)GaS] ₄	137	339	131	1.173
[(Et ₃ C)GaS] ₄	149	333	175	0.018
[(Me ₃ C)GaSe] ₄	119	305	116	3.668
[(EtMe ₂ C)GaSe] ₄	137	344	124	2.562
[(Et ₂ MeC)GaSe] ₄	147	359	136	0.815
[(Et ₃ C)GaSe] ₄	156	339	189	0.005

Table 2.8: Selected thermodynamic data for gallium chalcogenide cubane compounds determined from thermogravimetric analysis. Data from E. G. Gillan, S. G. Bott, and A. R. Barron, *Chem. Mater.*, 1997, **9**, 3, 796.

A common method used to enhance precursor volatility and corresponding efficacy for CVD applications is to incorporate partially (Figure 2.62b) or fully (Figure 2.62c) fluorinated ligands. As may be seen from Table 2.7 this substitution does results in significant decrease in the ΔH_{sub} , and thus increased volatility. The observed enhancement in volatility may be rationalized either by an increased amount of intermolecular repulsion due to the additional lone pairs or that the reduced polarizability of fluorine (relative to hydrogen) causes fluorinated ligands to have less intermolecular attractive interactions.

2.4.3.3 Determination of sublimation entropy

The entropy of sublimation is readily calculated from the ΔH_{sub} and the calculated T_{sub} data, (2.53).

$$\Delta S_{\text{sub}} = \frac{\Delta H_{\text{sub}}}{T_{\text{sub}}} \quad (2.53)$$

Table 2.7 and Table 2.8 show typical values for metal β -diketonate compounds and gallium chalcogenide cubane compounds, respectively. The range observed for gallium chalcogenide cubane compounds ($\Delta S_{\text{sub}} = 330 \pm 20$ J/K.mol) is slightly larger than values reported for the metal β -diketonates compounds ($\Delta S_{\text{sub}} = 130 - 330$ J/K.mol) and organic compounds (100 - 200 J/K.mol), as would be expected for a transformation giving translational and internal degrees of freedom. For any particular chalcogenide, i.e., [(R)GaS]₄, the lowest ΔS_{sub} are observed for the Me₃C derivatives, and the largest ΔS_{sub} for the Et₂MeC derivatives, see Table 2.8. This is in line with the relative increase in the modes of freedom for the alkyl groups in the absence of crystal packing forces.

2.4.3.4 Determination of vapor pressure

While the sublimation temperature is an important parameter to determine the suitability of a potential precursor compounds for CVD, it is often preferable to express a compound's volatility in terms of its vapor pressure. However, while it is relatively straightforward to determine the vapor pressure of a liquid or gas, measurements of solids are difficult (e.g., use of the isoteniscopic method) and few laboratories are equipped to perform such experiments. Given that TGA apparatus are increasingly accessible, it would therefore be desirable to have a simple method for vapor pressure determination that can be accomplished on a TGA.

Substitution of (2.49) into (2.51) allows for the calculation of the vapor pressure (p) as a function of temperature (T). For example, Figure 2.68 shows the calculated temperature dependence of the vapor pressure for $[(\text{Me}_3\text{C})\text{GaS}]_4$. The calculated vapor pressures at 150 °C for metal β -diketonates compounds and gallium chalcogenide cubane compounds are given in Table 2.7 and Table 2.8.

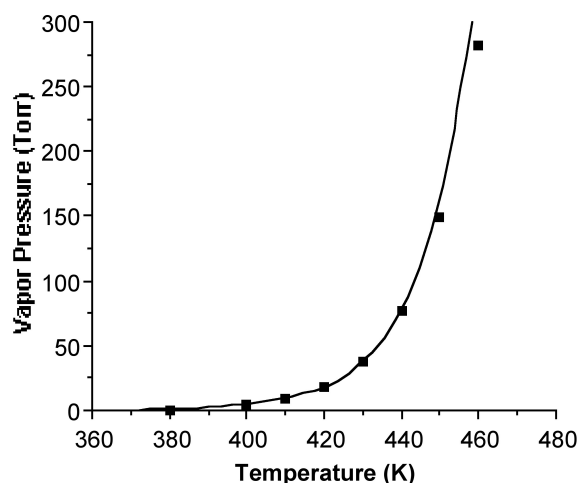


Figure 2.68: A plot of calculated vapor pressure (Torr) against temperature (K) for $[(\text{Me}_3\text{C})\text{GaS}]_4$. Adapted from E. G. Gillan, S. G. Bott, and A. R. Barron, *Chem. Mater.*, 1997, **9**, 3, 796.

The TGA approach to show reasonable agreement with previous measurements. For example, while the value calculated for $\text{Fe}(\text{acac})_3$ (2.78 Torr @ 113 °C) is slightly higher than that measured directly by the isoteniscopic method (0.53 Torr @ 113 °C); however, it should be noted that measurements using the sublimation bulb method obtained values much lower (8×10^{-3} Torr @ 113 °C). The TGA method offers a suitable alternative to conventional (direct) measurements of vapor pressure.

2.4.3.5 Bibliography

- P. W. Atkins, *Physical Chemistry*, 5th ed., W. H. Freeman, New York (1994).
- G. Beech and R. M. Lintonbon, *Thermochim. Acta*, 1971, **3**, 97.
- B. D. Fahlman and A. R. Barron, *Adv. Mater. Optics Electron.*, 2000, **10**, 223.
- E. G. Gillan, S. G. Bott, and A. R. Barron, *Chem. Mater.*, 1997, **9**, 3, 796.
- J. O. Hill and J. P. Murray, *Rev. Inorg. Chem.*, 1993, **13**, 125.
- J. P. Murray, K. J. Cavell and J. O. Hill, *Thermochim. Acta*, 1980, **36**, 97.
- M. A. V. Ribeiro da Silva and M. L. C. C. H. Ferrao, *J. Chem. Thermodyn.*, 1994, **26**, 315.
- R. Sabbah, D. Tabet, S. Belaadi, *Thermochim. Acta*, 1994, **247**, 193.

- L. A. Torres-Gomez, G. Barreiro-Rodriguez, and A. Galarza-Mondragon, *Thermochim. Acta*, 1988, **124**, 229.

2.5 Differential Scanning Calorimetry (DSC)¹⁶

2.5.1 Introduction

Differential scanning calorimetry (DSC) is a technique used to measure the difference in the heat flow rate of a sample and a reference over a controlled temperature range. These measurements are used to create phase diagrams and gather thermoanalytical information such as transition temperatures and enthalpies.

2.5.1.1 History

DSC was developed in 1962 by Perkin-Elmer employees Emmett Watson and Michael O'Neill and was introduced at the Pittsburgh Conference on Analytical Chemistry and Applied Spectroscopy (Figure 2.69). The equipment for this technique was available to purchase beginning in 1963 and has evolved to control temperatures more accurately and take measurements more precisely, ensuring repeatability and high sensitivity.

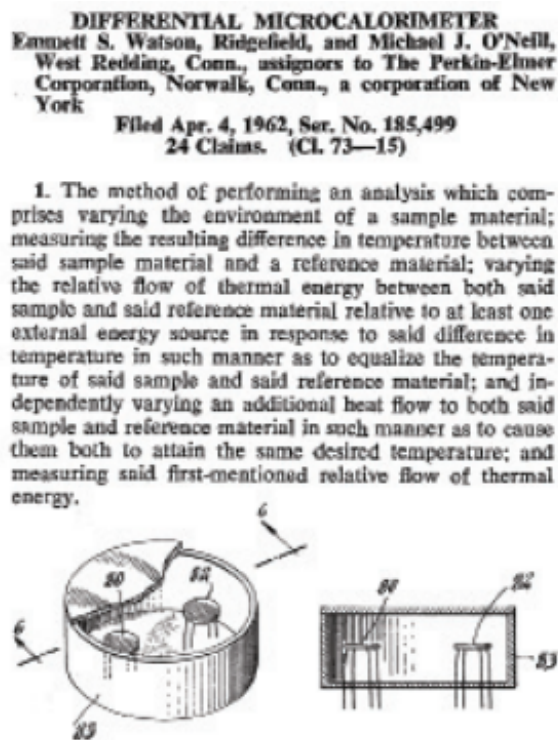


Figure 2.69: An excerpt from the original DSC patent.

¹⁶This content is available online at <<http://cnx.org/content/m43548/1.2/>>.

2.5.2 Theory

2.5.2.1 Phase transitions

Phase transitions refer to the transformation from one state of matter to another. Solids, liquids, and gasses are changed to other states as the thermodynamic system is altered, thereby affecting the sample and its properties. Measuring these transitions and determining the properties of the sample is important in many industrial settings and can be used to ensure purity and determine composition (such as with polymer ratios). Phase diagrams (Figure 2.70) can be used to clearly demonstrate the transitions in graphical form, helping visualize the transition points and different states as the thermodynamic system is changed.

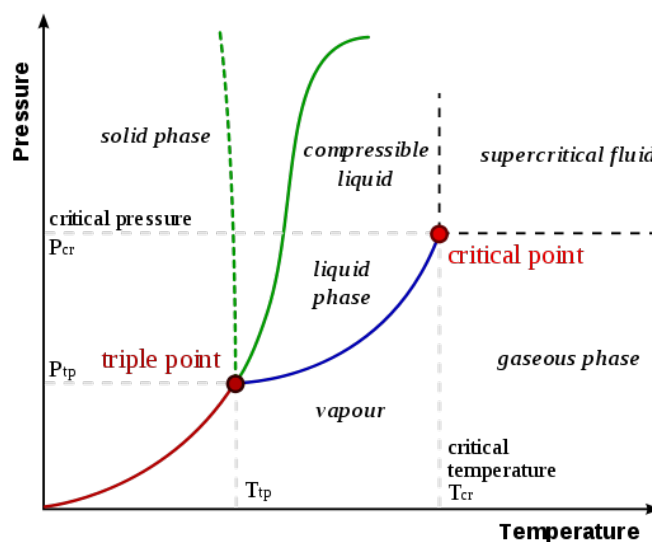


Figure 2.70: An example of a typical phase diagram.

2.5.2.2 Differential thermal analysis

Prior to DSC, differential thermal analysis (DTA) was used to gather information about transition states of materials. In DTA, the sample and reference are heated simultaneously with the same amount of heat and the temperature of each is monitored independently. The difference between the sample temperature and the reference temperature gives information about the exothermic or endothermic transition occurring in the sample. This strategy was used as the foundation for DSC, which sought to measure the difference in energy needed to keep the temperatures the same instead of measure the difference in temperature from the same amount of energy.

2.5.2.3 Differential scanning calorimeter

Instead of measuring temperature changes as heat is applied as in DTA, DSC measures the amount of heat that is needed to increase the temperatures of the sample and reference across a temperature gradient. The sample and reference are kept at the same temperature as it changes across the gradient, and the differing amounts of heat required to keep the temperatures synchronized are measured. As the sample undergoes

phase transitions, more or less heat is needed, which allows for phase diagrams to be created from the data. Additionally, specific heat, glass transition temperature, crystallization temperature, melting temperature, and oxidative/thermal stability, among other properties, can be measured using DSC.

2.5.3 Applications

DSC is often used in industrial manufacturing, ensuring sample purity and confirming compositional analysis. Also used in materials research, providing information about properties and composition of unknown materials can be determined. DSC has also been used in the food and pharmaceutical industries, providing characterization and enabling the fine-tuning of certain properties. The stability of proteins and folding/unfolding information can also be measured with DSC experiments.

2.5.4 Instrumentation

2.5.4.1 Equipment

The sample and reference cells (also known as pans), each enclosing their respective materials, are contained in an insulated adiabatic chamber (Figure 2.71). The cells can be made of a variety of materials, such as aluminum, copper, gold and platinum. The choice of which is dictated by the necessary upper temperature limit. A variable heating element around each cell transfers heat to the sample, causing both cells' temperature to rise in coordination with the other cell. A temperature monitor measures the temperatures of each cell and a microcontroller controls the variable heating elements and reports the differential power required for heating the sample versus the reference. A typical setup, including a computer for controlling software, is shown in Figure 2.72.

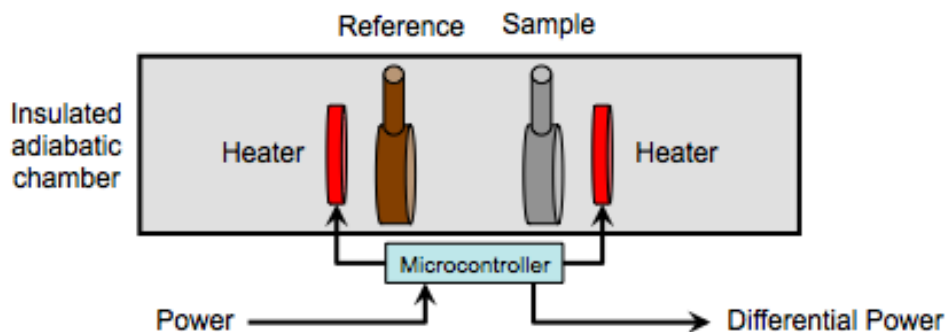


Figure 2.71: Diagram of basic DSC equipment.



Figure 2.72: Picture of a basic DSC setup in a laboratory.

2.5.4.2 Modes of operations

With advancement in DSC equipment, several different modes of operations now exist that enhance the applications of DSC. Scanning mode typically refers to conventional DSC, which uses a linear increase or decrease in temperature. An example of an additional mode often found in newer DSC equipment is an isothermal scan mode, which keeps temperature constant while the differential power is measured. This allows for stability studies at constant temperatures, particularly useful in shelf life studies for pharmaceutical drugs.

2.5.4.3 Calibration

As with practically all laboratory equipment, calibration is required. Calibration substances, typically pure metals such as indium or lead, are chosen that have clearly defined transition states to ensure that the measured transitions correlate to the literature values.

2.5.5 Obtaining measurements

2.5.5.1 Sample preparation

Sample preparation mostly consists of determining the optimal weight to analyze. There needs to be enough of the sample to accurately represent the material, but the change in heat flow should typically be between 0.1 - 10 mW. The sample should be kept as thin as possible and cover as much of the base of the cell as possible. It is typically better to cut a slice of the sample rather than crush it into a thin layer. The correct reference material also needs to be determined in order to obtain useful data.

2.5.5.2 DSC curves

DSC curves (e.g., Figure 2.73) typically consist of the heat flow plotted versus the temperature. These curves can be used to calculate the enthalpies of transitions, (ΔH), (2.54), by integrating the peak of the state transition, where K is the calorimetric constant and A is the area under the curve.

$$\Delta H = KA \tag{2.54}$$

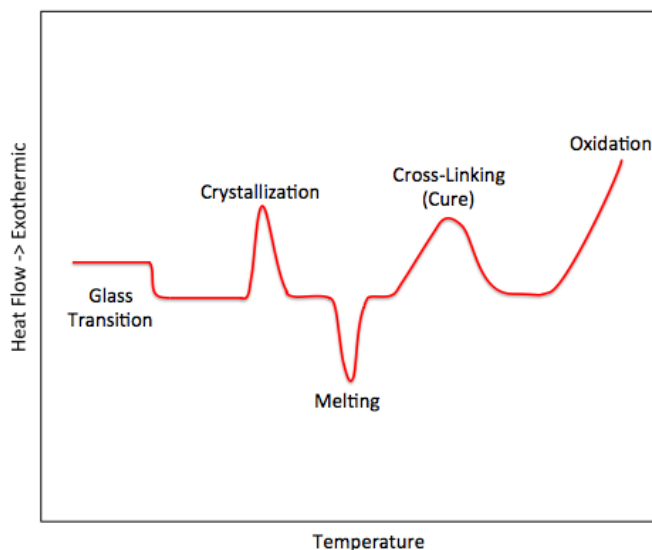


Figure 2.73: An idealized DSC curve showing the shapes associated with particular phase transitions.

2.5.5.3 Sources of error

Common error sources apply, including user and balance errors and improper calibration. Incorrect choice of reference material and improper quantity of sample are frequent errors. Additionally, contamination and how the sample is loaded into the cell affect the DSC.

2.5.6 Bibliography

- E. Watson, M. O'Neill, J. Justin, and N. Brenner, *Anal. Chem.*, 1964, **36**, 1233.
- E. Watson and M. O'Neill, U.S. Patent 3,263,484 (1966).
- G. Hohne, W. Hemminger, and H. Flammersheim, *Differential Scanning Calorimetry*, 2nd Ed, Springer, New York, (2003).
- V. Berstein and V. Egorov, *Differential Scanning Calorimetry of Polymers: Physics, Chemistry, Analysis, Technology*, Ellis Horwood, New York, (1994).
- J. Dean, *The Analytical Chemistry Handbook*; McGraw Hill: New York, (1995).
- E. Gmelin and St. M. Sarge, *Pure Appl. Chem.* 1995, **67**, 1789.

2.6 Introduction to Cyclic Voltammetry Measurements¹⁷

2.6.1 Introduction

Cyclic voltammetry (CV) is one type of potentiodynamic electrochemical measurements. Generally speaking, the operating process is a potential-controlled reversible experiment, which scans the electric potential before turning to reverse direction after reaching the final potential and then scans back to the initial potential, as shown in Figure 2.74a. When voltage is applied to the system changes with time, the current will change with time accordingly as shown in Figure 2.74b. Thus the curve of current and voltage, illustrated in Figure 2.74c, can be represented from the data, which can be obtained from Figure 2.74a and b.

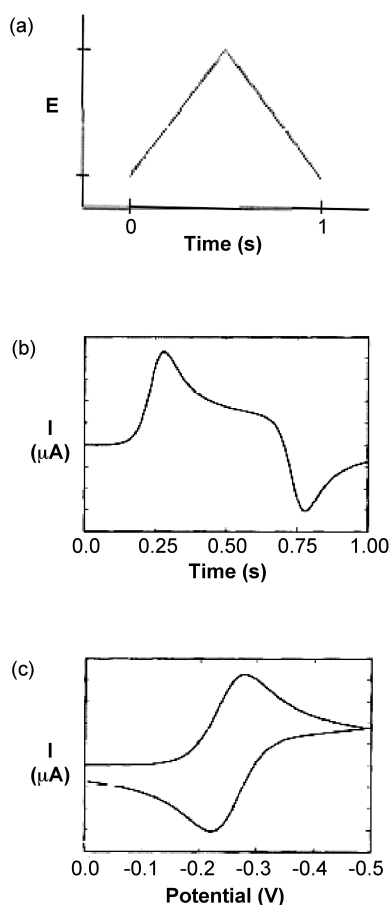


Figure 2.74: Potential wave changes with time (a); current response with time (b); current-potential representations (c). Adapted from D. K. Gosser, Jr. *Cyclic Voltammetry Simulation and Analysis of Reaction Mechanisms*, Wiley-VCH, New York, (1993).

Cyclic voltammetry is a very important analytical characterization in the field of electrochemistry. Any process that includes electron transfer can be investigated with this characterization. For example, the

¹⁷This content is available online at <<http://cnx.org/content/m34669/1.1/>>.

investigation of catalytical reactions, analyzing the stoichiometry of complex compounds, and determining of the photovoltaic materials' band gap. In this module, I will focus on the application of CV measurement in the field of characterization of solar cell materials.

Although CV was first practiced using a hanging mercury drop electrode, based on the work of Nobel Prize winner Heyrovský (Figure 2.75), it did not gain widespread until solid electrodes like Pt, Au and carbonaceous electrodes were used, particularly to study anodic oxidations. A major advance was made when mechanistic diagnostics and accompanying quantitations became known through the computer simulations. Now, the application of computers and related software packages make the analysis of data much quicker and easier.



Figure 2.75: Czech chemist and inventor Jaroslav Heyrovský (1890 – 1967).

2.6.2 The components of a CV system

As shown in Figure 2.76, the CV systems are as follows:

- The epsilon includes potentiostat and current-voltage converter. The potentiostat is required for controlling the applied potential, and a current-to-voltage converter is used for measuring the current, both of which are contained within the epsilon (Figure 2.76).
- The input system is a function generator (Figure 2.76). Operators can change parameters, including scan rate and scan range, through this part. The output part is a computer screen, which can show data and curves directly to the operators.
- All electrodes must work in electrolyte solution (Figure 2.76).
- Sometimes, the oxygen and water in the atmosphere will dissolve in the solution, and will be deoxidized or oxidized when voltage is applied. Therefore the data will be less accurate. To prevent this from happening, bubbling of an inert gas (nitrogen or argon) is required.
- The key component of the CV systems is the electrochemical cell (Figure 2.76), which is connected to the epsilon part. Electrochemical cell contains three electrodes, counter electrode (C in Figure 2.76), working electrode (W in Figure 2.76) and reference electrode (R in Figure 2.76). All of them must be immersed in an electrolyte solution when working.

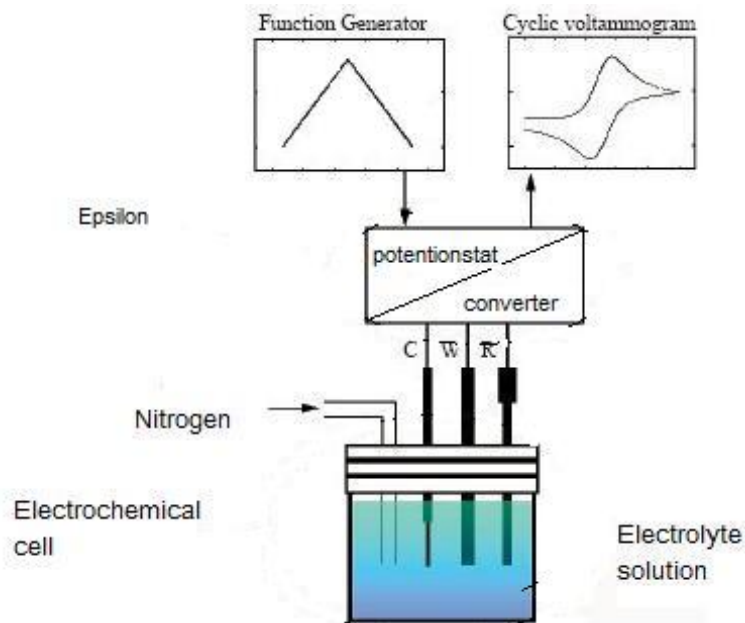


Figure 2.76: Components of cyclic voltammetry systems. Adapted from D. K. Gossler, Jr., *Cyclic Voltammetry Simulation and Analysis of Reaction Mechanisms*, Wiley-VCH, New York, (1993).

In order to better understand the electrodes mentioned above, three kinds of electrodes will be discussed in more detail.

- Counter electrodes (C in Figure 2.76) are non-reactive high surface area electrodes, for which the platinum gauze is the common choice.
- The working electrode (W in Figure 2.76) is commonly an inlaid disc electrodes (Pt, Au, graphite, etc.) of well-defined area are most commonly used. Other geometries may be available in appropriate circumstances, such as dropping or hanging mercury hemisphere, cylinder, band, arrays, and grid electrodes.
- For the reference electrode (R in Figure 2.76), aqueous Ag/AgCl or calomel half cells are commonly used, and can be obtained commercially or easily prepared in the laboratory. Sometimes, a simple silver or platinum wire is used in conjunction with an internal potential reference provided by ferrocene (Figure 2.77), when a suitable conventional reference electrode is not available. Ferrocene undergoes a one-electron oxidation at a low potential, around 0.5 V versus a saturated calomel electrode (SCE). It is also been used as standard in electrochemistry as $F_c^+/F_c = 0.64$ V versus a normal hydrogen electrode (NHE).

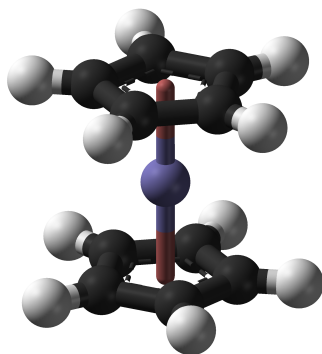


Figure 2.77: The structure of $(C_5H_5)_2Fe$ (ferrocene).

Cyclic voltammetry systems employ different types of potential waveforms (Figure 2.78) that can be used to satisfy different requirements. Potential waveforms reflect the way potential is applied to this system. These different types are referred to by characteristic names, for example, cyclic voltammetry, and differential pulse voltammetry. The cyclic voltammetry analytical method is the one whose potential waveform is generally an isosceles triangle (Figure 2.78a).

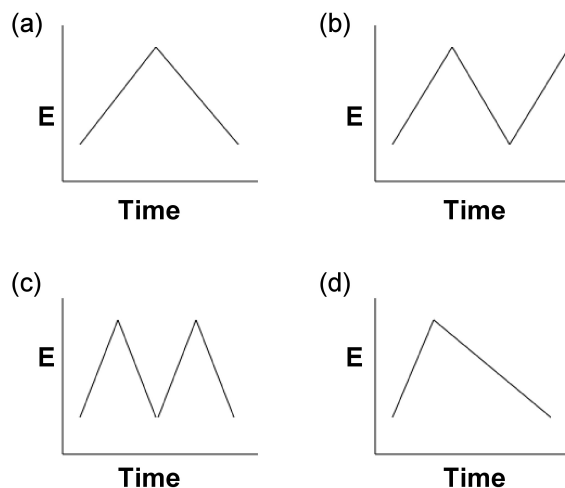


Figure 2.78: Examples of different waveforms of CV systems, illustrating various possible cycles. Adapted from D. K. Gosser, Jr., *Cyclic Voltammetry Simulation and Analysis of Reaction Mechanisms*, Wiley-VCH, New York (1993).

2.6.3 The physical principles on which the CV systems are based

As mentioned above, there are two main parts of a CV system: the electrochemical cell and the epsilon. Figure 2.79 shows the schematic drawing of circuit diagram in electrochemical cell.

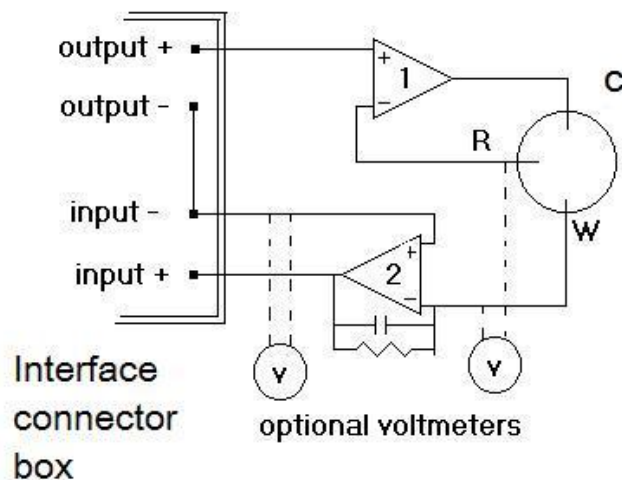


Figure 2.79: Diagram of a typical cyclic voltammetry circuit layout. Adapted from R. G. Compton and C. E. Banks, *Understanding Voltammetry*, World Scientific, Singapore (2007).

In a voltammetric experiment, potential is applied to a system, using working electrode (W in Figure 2.79) and the reference electrode (R = Figure 2.79), and the current response is measured using the working electrode and a third electrode, the counter electrode (C in Figure 2.79). The typical current-voltage curve for ferricyanide/ferrocyanide, (2.55), is shown in Figure 2.80.



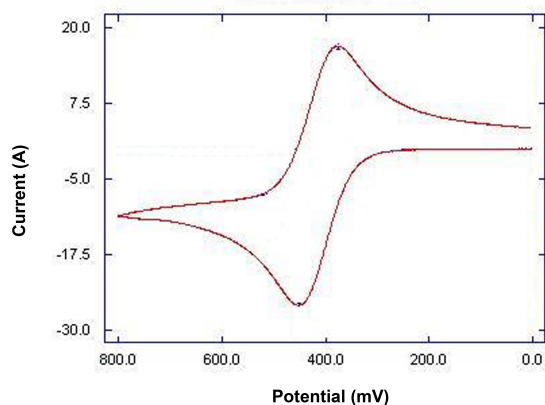


Figure 2.80: Typical curve of current-voltage curve for for ferricyanide/ferrocyanide, (2.55).

2.6.3.1 What useful information we can get from the data collected

The information we are able to obtain from CV experimental data is the current-voltage curve. From the curve we can then determine the redox potential, and gain insights into the kinetics of electron reactions, as well as determine the presence of reaction intermediate.

2.6.4 Why choose CV for the characterizations of solar cell materials?

Despite some limitations, cyclic voltammetry is very well suited for a wide range of applications. Moreover, in some areas of research, cyclic voltammetry is one of the standard techniques used for characterization. Due to its characteristic shapes of curves, it has been considered as ‘electrochemical spectroscopy’. In addition, the system is quite easy to operate, and sample preparation is relatively simple.

The band gap of a semiconductor is a very important value to be determined for photovoltaic materials. Figure 2.81 shows the relative energy level involved in light harvesting of an organic solar cell. The energy difference (E_g) between the lowest unoccupied molecular orbital (LUMO) and the highest occupied molecular orbital (HOMO), which determines the efficiency. The oxidation and reduction of an organic molecule involve electron transfers (Figure 2.82), and CV measurements can be used to determine the potential change during redox. Through the analysis of data obtained by the CV measurement the electronic band gap is obtained.

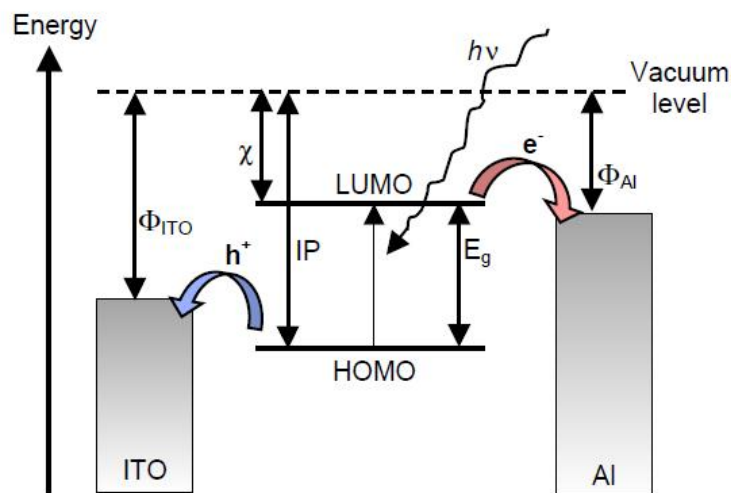


Figure 2.81: Diagram showing energy level and light harvesting of an organic solar cell. Adapted from S. B. Darling, *Energy Environm. Sci.*, 2009, 2, 1266.

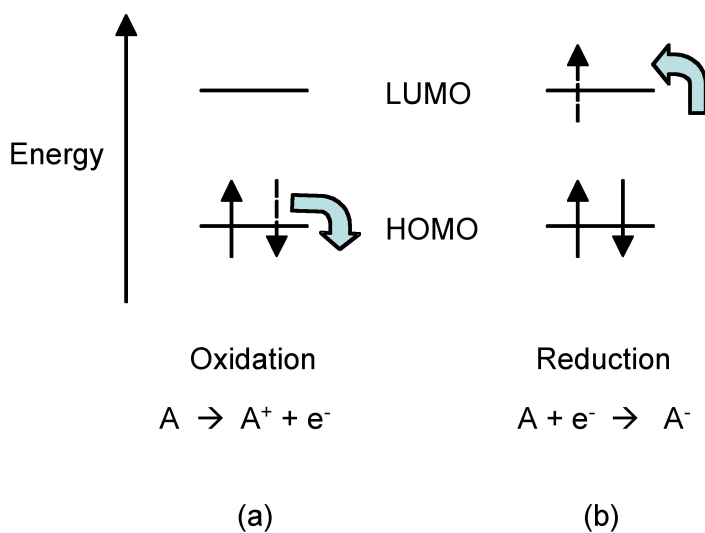


Figure 2.82: Diagram showing energy level and light harvesting of organic solar cell. Adapted from D. K. Gosser, Jr., *Cyclic Voltammetry Simulation and Analysis of Reaction Mechanisms*, Wiley-VCH, New York (1993).

2.6.4.1 The example of the analysis of CV data in solar cell material characterization

Graphene nanoribbons (GNRs) are long, narrow sheets of graphene formed from the unzipping of carbon nanotubes (Figure 2.83). GNRs can be both semiconducting and semi-metallic, depending on their width, and they represent a particularly versatile variety of graphene. The high surface area, high aspect ratio, and interesting electronic properties of GNRs render them promising candidates for applications of energy-storage materials.

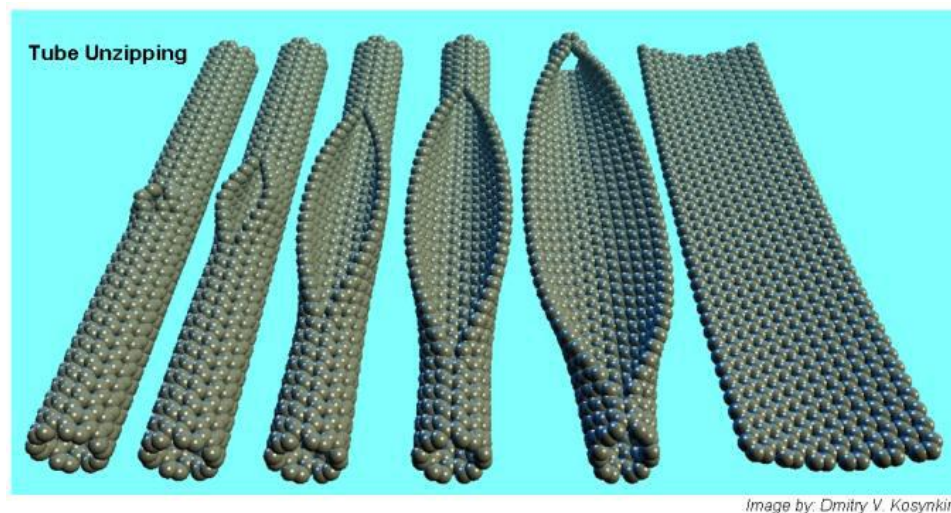


Figure 2.83: Schematic for the “unzipping” of carbon nanotubes to produce graphene (Rice University).

Graphene nanoribbons can be oxidized to oxidized graphene nanoribbons (XGNRs), are readily soluble in water easily. Cyclic voltammetry is an effective method to characterize the band gap of semiconductor materials. To test the band gap of oxidized graphene nanoribbons (XGNRs), operating parameters can be set as follows:

- 0.1M KCl solution
- Working electrode: evaporated gold on silicon.
- Scan rate: 10 mV/s.
- Scan range: 0 ~ 3000 mV for oxidization reaction; -3000 ~ 0 mV for reduction reaction.
- Samples preparation: spin coat an aqueous solution of the oxidized graphene nanoribbons onto the working electrode, and dry at 100 °C.

To make sure that the results are accurate, two samples can be tested under the same condition to see whether the redox peaks are at the same position. The amount of XGNRs will vary from sample to sample, thus the height of peaks will vary also. Typical curves obtained from the oxidation reaction (Figure 2.82a) and reduction reaction (Figure 2.82b) are shown in Figure 2.84 and Figure 2.85, respectively.

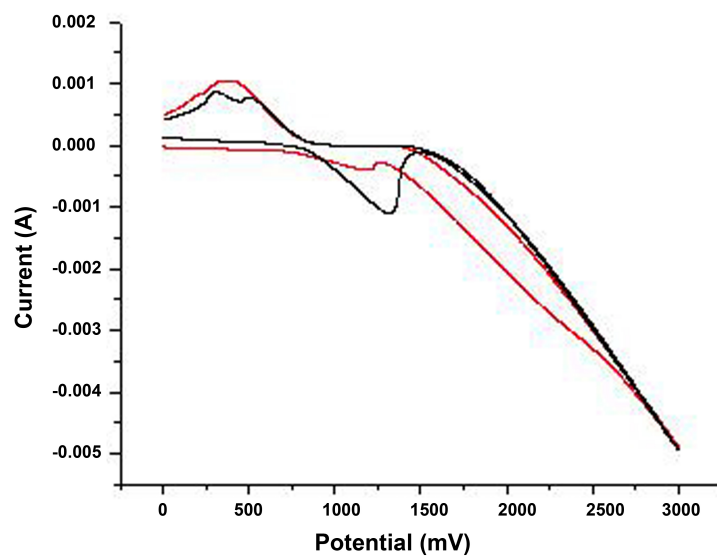


Figure 2.84: Oxidation curves of two samples of XGNRs prepared under similar condition. The sample with lower concentration is shown by the red curve, while the sample with higher concentration is shown as a black curve.

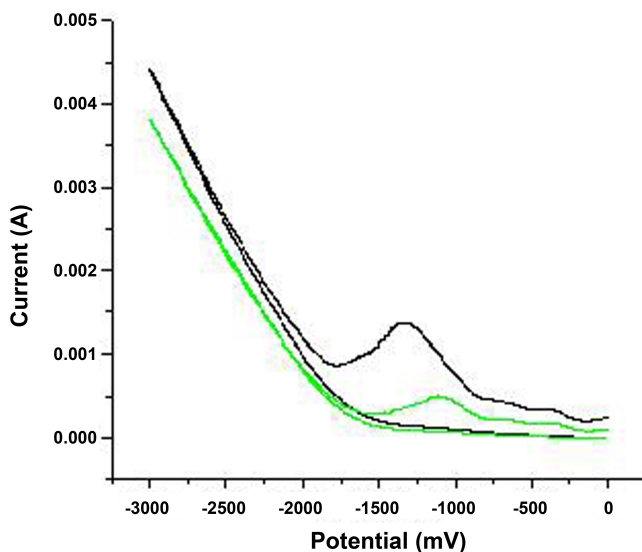


Figure 2.85: Reduction curves of two samples of XGNRs prepared under similar condition. The sample with lower concentration is shown by the green curve, while the sample with higher concentration is shown as a black curve.

From the curves shown in Figure 2.84 and Figure 2.85 the following conclusions can be obtained:

- Two reduction peak and onset is about -0.75 V (i.e., Figure 2.82b).
- One oxidation peak with onset about 0.85 V (i.e., Figure 2.82a).
- The calculated band gap = 1.60 eV.

In conclusion, there are many applications for CV system, efficient method, and the application in the field of solar cell provides the band gap information for research.

2.6.5 Bibliography

- R. N. Adams, *Electrochemistry at Solid Electrodes*, Marcel Dekker, NewYork (1968).
- R. G. Compton, and C. E. Banks, *Understanding Voltammetry*, World Scientific, Singapore, (2007).
- S. B. Darling, *Energy Environm. Sci.*, 2009, **2**, 1266.
- S. W. Feldberg, *A General Method for Simulation*, Vol. 3 in Electroanalytical Chemistry Series, Marcel Dekker, NewYork, (1969).
- W. Kemula and Z. Kublik, *Nature*, 1958, **182**, 793.
- D. V. Kosynkin, A. L Higginbotham, A. Sinitskii, J. R. Lomeda, A. Dimiev, B. K. Price, and J. M. Tour, *Nature*, 2009, **458**, 872.
- R. S. Nicholson and I. Shain, *Anal. Chem.*, 1964, **36**, 706.
- L. Piszczek, A. Lgnatowicz, J. Kielbase, *J. Chem. Edu.*, 1998, **65**, 171.
- J. Zhu, Z. Zhao, D. Xiao, J. Li, X. Yang, and Y. Wu, *Electrochem. Commun.*, 2005, **7**, 58.

2.7 Determination of Relaxation Parameters of Contrast Agents¹⁸

2.7.1 Introduction

Magnetic resonance imaging (MRI) (also known as nuclear magnetic resonance imaging (NMRI) or magnetic resonance tomography (MRT)) is a powerful noninvasive diagnostic technique, which is used to generate magnetic field (B_0) and interacts with spin angular momentum of the nucleus in the tissue. Spin angular momentum depends on number of protons and neutrons of nucleus. Nuclei with even number of protons plus neutrons are insensitive to magnetic field, so cannot be viewed by MRI.

Each nucleus can be considered as an arrow with arbitrary direction in absence of external magnetic field (Figure 2.86). And we consider them to get oriented in same direction once magnetic field applied (Figure 2.87). In order to get nuclei orient in specific direction, energy is supplied, and to bring it to original position energy is emitted. All this transitions eventually lead to changes in angular velocity, which is defined as Larmor frequency and the expression (2.56), where ω is the Larmor frequency, γ is the gyromagnetic ratio, and B_0 is the magnetic field. It is not easy to detect energy, which is involved in such a transition, that's why use of high resolution spectrometers required, those which are developed by nowadays as a most powerful MRI are close to 9 Tesla with mass approaching forty five tons. Unfortunately it is expensive tool to purchase and to operate. That's why new techniques should be developed, so most of the MRI spectrometers can be involved in imaging. Fortunately presence of huge amount of nuclei in analyzed sample or body can provide with some information.

$$\omega = \gamma B_0 \tag{2.56}$$

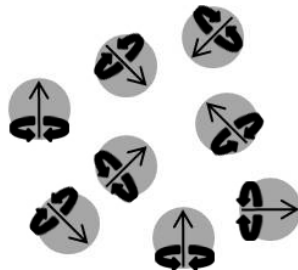


Figure 2.86: Representation of nuclei in absence of magnetic field.

¹⁸This content is available online at <<http://cnx.org/content/m38342/1.1/>>.

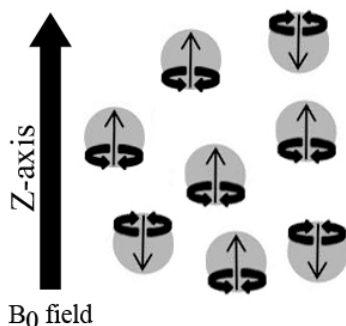


Figure 2.87: Representation of nuclei in presence of magnetic field.

2.7.1.1 Nuclear magnetic resonance relaxometer

Each nucleus possesses microscopic magnetic spins of x , y and z . Presence of randomly distributed atoms with varying x and y spins will lead to zero upon summation of x and y planes. But in case of z , summation of magnetic spins will not lead to cancellation. According to Currie's law, (2.57), (M_z is the resulting magnetization of z axis, C is a material specific Curie constant, B_0 is the magnetic field, and T is absolute temperature), magnetization of z axis proportional to magnetic field applied from outside. Basically, excitation happens by passing current through coil which leads to magnetization of x , y and z axis. It is the way of changing magnetism from z axis to x and y axis. Once external current supply is turned off, magnetization will eventually quench. This means a change of magnetization from x and y axis to z axis, were it eventually become equilibrated and device no more can detect the signals. Energy which is emitted from excited spin leads to development of new current inside of the same coil recorded by detector; hence same coil can be used as detector and source of magnetic field. This process called as a relaxation and that's why, return of magnetization to z axis called as spin-lattice relaxation or T_1 relaxation (time required for magnetization to align on z axis). Eventual result of zero magnetization on x and y axis called as spin-spin relaxation or T_2 relaxation (Figure 2.88).

$$M_z = CB_0/T \quad (2.57)$$

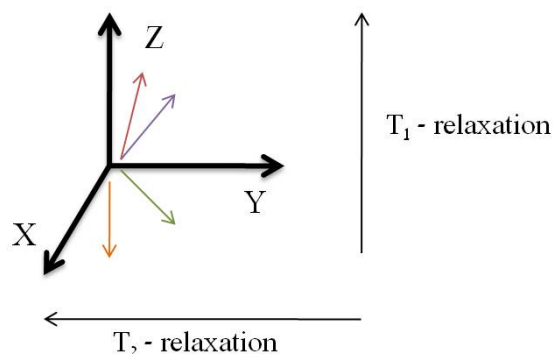


Figure 2.88: Magnetic spins relaxation mechanism

2.7.2 Contrast agents for MRI

In MRI imaging contrast is determined according to T_1 , T_2 or the proton density parameter. Therefore we can obtain three different images. By changing intervals between radio frequency (RF) 90° pulses and RF 180° pulses, the desired type of image can be obtained. There are few computational techniques available to improve contrast of image; those are repetitive scans and different mathematical computations. Repetitive scans take a long time, therefore cannot be applied in MRI. Mathematical computation on their own, do not provide with desired results. For that reason, in order to obtain high resolution images, contrast agents (CA) are an important part of medical imaging.

2.7.2.1 Types of contrast agents

There are different types of contrast agents available in markets which reduce the supremacy of T_1 or T_2 , and differentiate according to relaxivity₁ (r_1) and relaxivity₂ (r_2) values. The relaxivity (r_i) can be described as $1/T_i$ (s^{-1}) of water molecules per mM concentration of CA. Contrast agents are paramagnetic and can interact with dipole moments of water molecules, causing fluctuations in molecules. This theory is known as Solomon-Bloembergen-Morgan (SBM) theory. Those which are efficient were derivatives of gadolinium (e.g., gadobenic acid (FIGURE a) and gadoxetic acid (FIGURE b)), iron (e.g., superparamagnetic iron oxide and ultrasmall superparamagnetic iron oxide) and manganese (e.g., manganese dipyridoxal diphosphate). Fundamentally the role of contrast agents can be played by any paramagnetic species.

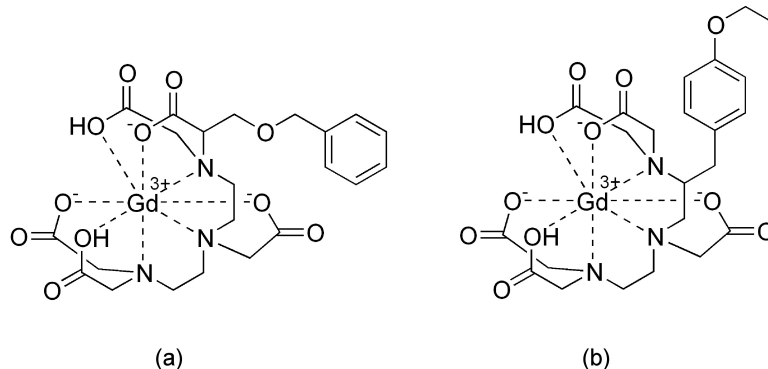


Figure 2.89: The structures of two representative commercial gadolinium MRI contrast agents; (a) gadobenic acid and (b) gadoxetic acid.

2.7.2.2 Principal of interactions of CA with surrounding media

There are two main principles of interactions of contrast agents with water molecules. One is direct interaction, which is called inner sphere relaxation, and the other mechanism that happens in the absence of direct interaction with water molecule which is outer sphere relaxation. If we have water molecules in the first coordination sphere of metal ion, we can consider them as the inner sphere, and if diffusion of protons from outside happens randomly we define them as outer sphere relaxation. Another type of relaxivity comes from already affected water molecules, which transfers their relaxivity to protons of close proximity, this type of relaxivity called second sphere and is usually neglected or contributed as outer sphere. In inner sphere proton relaxivity there are two main mechanisms involved in relaxation. One is dipole-dipole interactions between metal and proton and another is scalar mechanism. Dipole-dipole interaction affects electron spin vectors and scalar mechanism usually controls water exchange. Effect of contrast agents on T_1 relaxation is much larger than on T_2 , since T_1 is much larger for tissues than T_2 .

2.7.3 Determination of relaxivity

Determination of relaxivity became very easy with the advancements of NMR and computer technology, where you need just to load your sample and read values from the screen. But let's consider in more detail what are the precautions should be taken during sample preparation and data acquisition.

2.7.3.1 Sample preparation

The sample to be analyzed is dissolved in water or another solvent. Generally water is used since contrast agents for medical MRI are used in aqueous media. The amount of solution used is determined according to the internal standard volume, which is used for calibration purposes of device and is usually provided by company producing device. A suitable sample holder is a NMR tube. It is important to degas solvent prior measurements by bubbling gas through it (nitrogen or argon works well), so no any traces of oxygen remains in solution, since oxygen is paramagnetic.

2.7.3.2 Data acquisition

Before collecting data it is better to keep the sample in the device compartment for few minutes, so temperature of magnet and your solution equilibrates. The relaxivity (r_i) calculated according to ((2.58)), where T_i is the relaxation time in the presence of CAs, T_{id} is the relaxation time in the absence of CAs, and CA is the concentration of paramagnetic CAs (mM). Having the relaxivity values allows for a comparison of a particular compound to other known contrast agents.

$$r_i = (1/T_i - 1/T_{id})/[CA] \quad (2.58)$$

2.7.4 Bibliography

- D. Canet, *Nuclear Magnetic Resonance: Concepts and Methods*, John Wiley and Sons, Chichester (1996).
- A. Abragam, *Principles of Nuclear Magnetism*, Oxford University Press, Oxford (1961).
- I. Solomon and N. Bloembergen, *J. Chem. Phys.*, 1956, **25**, 261.
- N. Bloembergen and L. O. Morgan, *J. Chem. Phys.*, 1961, **34**, 842.
- P. G. Morris and P. Mansfield, *NMR Imaging in Biomedicine*, Academic Press, Orlando (1982).
- J. S. Ananta, B. Godin, R. Sethi, L. Moriggi, X. Liu, R. E. Serda, R. Krishnamurthy, R. Muthupillai, R. D. Bolskar, L. Helm, M. Ferrari, L. J. Wilson, and P. Decuzzi, *Nature Nanotech.*, 2010, **5**, 817.
- R. B. Lauffer, *Chem. Rev.*, 1987, **87**, 901.

Solutions to Exercises in Chapter 2

Solution to Exercise 2.2.1.1 (p. 135)

$$m = \Delta T_f / K_f \text{ water} \quad (2.59)$$

$$m = 0.445 \text{ }^\circ\text{C} / 1.86 \text{ }^\circ\text{C.kg/mol} \quad (2.60)$$

$$m = 0.239 \text{ mol} \quad (2.61)$$

Solution to Exercise 2.2.1.2 (p. 135)

$$M_w = K_f (\text{g solute}) / \Delta T_f (\text{kg solvent}) \quad (2.62)$$

$$M_w = \frac{1.86 \text{ }^\circ\text{C.kg/moles (1.200 g)}}{0.445 \text{ }^\circ\text{C (0.03056 kg)}} \quad (2.63)$$

$$M_w = 164 \text{ g/mol} \quad (2.64)$$

Solution to Exercise 2.2.1.3 (p. 135)

$$\Delta T_f = K_f(m)i \quad (2.65)$$

$$\Delta T_f = 1.86 \text{ }^\circ\text{C.kg/moles} \times 0.500 \text{ molal} \times 3 \quad (2.66)$$

$$\Delta T_f = 2.79 \text{ }^\circ\text{C} \quad (2.67)$$

Solution to Exercise 2.2.1.4 (p. 135)

$$g (\text{solute}) = M_w \times \Delta T_f \times (\text{kg solvent}) / K_f \quad (2.68)$$

$$g (\text{solute}) = \frac{164.0 \text{ g/mol (2.79 }^\circ\text{C) 0.06 kg}}{1.86 \text{ }^\circ\text{C.kg/moles}} \quad (2.69)$$

$$g (\text{solute}) = 14.76 \text{ g of Ca(NO}_3)_2 \quad (2.70)$$

Solution to Exercise 2.2.2.1 (p. 138)

$$M_w = \frac{(9 \text{ mol} \times (30,000 \text{ g/mol})^2) + (5 \text{ mol} \times (50,000 \text{ g/mol})^2)}{(9 \text{ mol} \times 30,000 \text{ g/mol}) + (5 \text{ mol} \times 50,000 \text{ g/mol})} = 40,000 \text{ g/mol}$$

Solution to Exercise 2.2.2.2 (p. 138)

$$M_z = \frac{(10 \text{ mol} \times (20,000 \text{ g/mol})^3) + (2 \text{ mol} \times (50,000 \text{ g/mol})^3)}{(10 \text{ mol} \times (20,000 \text{ g/mol})^2) + (2 \text{ mol} \times (50,000 \text{ g/mol})^2)} = 100,000 \text{ g/mol}$$